

Multiple axon tracking for biohybrid brain computer interfaces from directional living neural networks

Thesis Subtitle

Author Name

A thesis presented for the degree of
Doctor of Philosophy

Department Name

University Name

Country

Date

1 Abstract

Lorem ipsum dolor sit amet, consectetur adipisicing elit, sed do eiusmod tempor incididunt ut labore et dolore magna aliqua. Ut enim ad minim veniam, quis nostrud exercitation ullamco laboris nisi ut aliquip ex ea commodo consequat. Duis aute irure dolor in reprehenderit in voluptate velit esse cillum dolore eu fugiat nulla pariatur. Excepteur sint occaecat cupidatat non proident, sunt in culpa qui officia deserunt mollit anim id est laborum. Lorem ipsum dolor sit amet, consectetur adipisicing elit, sed do eiusmod tempor incididunt ut labore et dolore magna aliqua. Ut enim ad minim veniam, quis nostrud exercitation ullamco laboris nisi ut aliquip ex ea commodo consequat. Duis aute irure dolor in reprehenderit in voluptate velit esse cillum dolore eu fugiat nulla pariatur. Excepteur sint occaecat cupidatat non proident, sunt in culpa qui officia deserunt mollit anim id est laborum. Lorem ipsum dolor sit amet, consectetur adipisicing elit, sed do eiusmod tempor incididunt ut labore et dolore magna aliqua. Ut enim ad minim veniam, quis nostrud exercitation ullamco laboris nisi ut aliquip ex ea commodo consequat. Duis aute irure dolor in reprehenderit in voluptate velit esse cillum dolore eu fugiat nulla pariatur. Excepteur sint occaecat cupidatat non proident, sunt in culpa qui officia deserunt mollit anim id est laborum.

Contents

| | |
|---|-----------|
| 1 Abstract | 1 |
| 2 Introduction | 5 |
| 2.1 Outline | 6 |
| 2.2 Biohybrid neural interfaces | 6 |
| 2.3 Engineered directional neural networks | 8 |
| 2.4 Multiple object tracking | 9 |
| 3 Methods and Materials | 10 |
| 3.1 Experimental procedures | 10 |
| 3.1.1 Dish preparation | 10 |
| 3.1.2 Poly-D-Lysine & laminin coating | 10 |
| 3.1.3 PDMS micro structure design, fabrication & mounting | 11 |
| 3.1.4 Retina dissection | 12 |
| 3.1.5 Spheroid creation | 12 |
| 3.1.6 Seeding PDMS micro structures | 12 |
| 3.1.7 Timelapse recording & image acquisition | 13 |
| 3.2 Data analysis | 13 |
| 3.2.1 Timelapse datasets | 13 |
| 3.2.2 Initial timelapse processing | 14 |
| 3.2.3 Axon growth cone labelling | 14 |
| 3.2.4 Timelapse data preprocessing | 15 |
| 3.2.5 Growth cone detection model | 15 |
| 3.2.5.1 Temporal context frames | 15 |
| 3.2.5.2 Tiling | 15 |
| 3.2.5.3 Detection output format | 17 |
| 3.2.5.4 Training procedure | 17 |
| 3.2.5.5 Data association | 18 |
| 3.2.6 Directionality inference from tracking | 18 |
| 4 Results | 20 |
| 4.1 Tracking performance | 20 |
| 4.2 Micro structure designs | 20 |
| 4.3 Between dataset variance | 20 |
| 4.4 Axonal viability across datasets & designs | 22 |
| 4.5 Directionality in PDMS designs | 23 |
| 4.6 Axon guidance design primitives | 26 |
| 5 Discussion | 28 |
| 5.1 Model architecture and generalization | 28 |
| 6 Supplementary Information | 29 |

List of Figures

| | | |
|---|---|----|
| 1 | Growth cone detection model overview | 16 |
| 2 | Growth cone tracking model performance | 21 |
| 3 | PDMS micro structure designs | 22 |
| 4 | Between dataset variance and axonal viability | 24 |
| 5 | Directionality in PDMS designs | 25 |
| 6 | Screening of PDMS design primitives | 27 |

List of Supplementary Figures

| | | |
|---|--|----|
| 1 | Initial timelapse preprocessing steps | 30 |
| 2 | Axon growth cone labelling | 31 |
| 3 | Labelled training data examples | 32 |
| 4 | Axon reconstruction from growth cone track | 33 |
| 5 | Axonal growth velocity | 33 |
| 6 | Axon outgrowth frequency | 34 |
| 7 | Number of axons stagnating | 34 |

List of Tables

| | | |
|---|--|----|
| 1 | RGC medium composition | 11 |
| 2 | Overview of timelapse recording data | 13 |
| 3 | Minimum cost flow hyperparameters | 19 |

List of Abbreviations

CLSM - Confocal laser scanning microscope PDMS CNN MOTA
DI deionized PDL PBS phosphate buffered saline CAD
CNS DBS
MEA
dLGN
MOT
R-CNN
IQR inter quartile range
AAV
GFP

2 Introduction

Broad scope approach-motivation statement

Funnel into short abstract-like summary of the project

background in three sections: biohybrid BCI, directional networks, MOT

research problem, research aims + presented solution, significance + which value

Why do we need directional neural networks? general entry funnel biohybrid interfaces disease models (sprinkle of bottom up neuroscience)

which efforts have been made to make networks directional? orient to csabas paper

Which solution does this work provide? primitives screen 20 test structures screen

2.1 Outline

Understanding the human brain requires neuroscience to develop complexity reducing model systems that capture relevant functional, anatomical or chemical features. The evaluation of which abstraction level and thus model system is appropriate for answering key functional questions about the brain has long been a source of controversy. This discussion is fundamentally rooted in the tension between losing essential features in overly simplified model systems, and dealing with overwhelming complexity and low experimental throughput in model systems more closely resembling the human brain.

Although this work broadly employs *in vitro* model systems thus trading off resemblance to real brains for higher throughput and reduced complexity, it is not primarily motivated by a certainty that this high abstraction level will indeed *solve* fundamental neuroscientific questions. Instead, this project aims to follow an approach that has led to notable progress in other domains, most prominently artificial intelligence: Developing an understanding of the system by engineering it. This method has found adoption in domains as neuromorphic engineering (Mead 1989) and neural engineering (Durand 2006), with the latter focusing i.a. on building technology from living neural systems. Guided by the engineering problems, the hope of these domains is that relevant neuroscientific questions are answered along the way. And even if this does not come true, advancement in these fields may still result in useful new technologies. The science presented here follows this pursuit.

You can only do engineering at that scale. that's why were at that scale. DId you make that clear enough? Inconsistency: you mention this here in the beginning but this idea is not really found throughout the introduction. Motivation is put on bad stimulation ability, and bad *in vitro* network models.

In this work, ... [abstract like but shorter] f

f
f
f
f
f
f
f

2.2 Biohybrid neural interfaces

Neuroelectric interfacing based on metal electrodes has made remarkable progress over the last decades (Maynard, Nordhausen, and Normann 1997, Jun et al. 2017). These technologies excel at locally confined high resolution neural recording for a time period on the order of weeks. However, given the immense challenges related to high quality neural interfacing (Stevenson and Kording 2011), naturally, existing recording and particularly stimulation technology exhibit shortcomings. The clinically most adapted CNS stimulation method, deep brain stimulation (DBS), does not specifically depolarize single neurons but instead exerts various modulatory effects on entire brain areas (Herrington, Cheng, and Eskandar 2016). Low spatiotemporal resolution may be tolerable for common DBS applications, however, addressing the clinically highly relevant cases of vision-, touch-, or hearing loss is currently limited by insufficient resolution (Tong et al. 2020). Another issue affecting both stimulation and conventional neural recording systems is the

induced foreign body response. Due to natural brain movement, rigid metal electrodes cause inflammation, neuronal cell death and glia formation while simultaneously, conventional electrode insulation undergoes biodegradation resulting in decreased impedance (Tresco and Winslow 2011, Saxena et al. 2013, Grill, Norman, and Bellamkonda 2009, Polikov, Tresco, and Reichert 2005). In research applications, central nervous system (CNS) stimulation is most commonly performed through optogenetic tools (Zemelman et al. 2002, Boyden et al. 2005). While the cell-type specificity of optogenetics can be of great value, the limitations in spatial resolution inherent to *in vivo* light-based technology seem to be a major hurdle for increasing spatial resolution. On top of this, the risk of genetic off-target effects and adeno associated virus (AAV) immune responses restrict medical use cases in the near term (Mendoza, El-Shamayleh, and Horwitz 2017).

Biohybrid implants take a fundamentally different approach to neural interfacing, drawing inspiration from tissue engineering and *in vitro* neuroscience. First described by Stieglitz et al. 2002, this promising technology aims to solve the latent issue of biocompatibility by moving towards the integration of biological components (Rochford et al. 2020). At the same time, biohybrid technology may benefit from the highly impressive *spec sheet* of a neuron, including energy efficiency, self-containment, and signal transmission properties. Whilst engineering with neural tissue presents almost daunting challenges, the biocompatibility prospects of biohybrid interfaces are currently unaccessible by competing technologies. CNS applications of the biohybrid approach include the coating of metal electrodes with host cells (Purcell et al. 2009, Faveri et al. 2014), and the use of ectopic axons as electrodes (Tang-Schomer et al. 2014, Adewole et al. 2021). The currently most advanced biohybrid implant is based on a hydrogel microcolumn containing ectopic cortical axons that are optogenetically driven through an light emitting diode (LED) optical fiber outside the brain (Adewole et al. 2021). While synapse formation was shown anatomically *in vitro*, the *in vivo* proof-of-concept implantation did not go as far as showing functional target tissue innervation.

Current biohybrid implants trade off biocompatibility for interface bandwidth and control. For example, the biohybrid implant presented in Adewole et al. 2021 relied on optically exciting the entire ectopically grown neural population, resulting in limited control of delivered stimulation. While this spatial resolution may be sufficient for specific use cases, this implant design offers insufficient control for delivering high dimensional data, such as sensory input. For addressing the pressing issue of functionally restoring sensory modalities (Bourne et al. 2021), a biohybrid implant needs to allow for stimulating independent channels. To solve this crucial design requirement, the implant presented here is based on a PDMS micro fluidic system enabling the independent stimulation of axons grown in micro channels. Briefly, PDMS membranes are placed on coated glass dishes and seeded with RGC spheroids. Axons extend through the 6 μm high channel system until they reach the 3 mm long output channel which will eventually be implanted. The final device will utilise stretchable AuTiO₂ nanowire electrical contact pads for stimulating RGC axons (Tybrandt et al. 2018). Long term host cell survival will be ensured by having the implant face the brain surface such that RGC spheroids are integrated with the CNS microenvironment. The device will be implanted targeting the dorsal lateral geniculate nucleus (dLGN). (illustration needed)

2.3 Engineered directional neural networks

It is well established that the connectivity within biological neural networks is a major determinant of the emerging electrophysiological dynamics. For example, the microcircuit of the cat visual cortex exhibits a high degree of sparsity with predominantly local inhibitory-, and excitatory connections to achieve its output (Douglas and Martin 1991). Despite the general agreement on the significance of neural circuits, the vast majority of in vitro models remain limited to random connectivity schemes. Neglecting this property of in vivo neural networks may be well justified in studies that focus on basic biological properties, for example in response to drug admission. However, any model system investigating higher level functional properties emerging at the circuits-level (e.g. learning mechanisms) requires confined connectivity.

More elaborately controlled connectivity schemes are indispensable for technology relying on living neural circuits. Biohybrid interfaces as described above rely fundamentally on directional connectivity. Innervation of neighboring RGC source wells may result in activity dynamics independent of the imposed electrical stimulation pattern, rendering single stimulation channels or the entire device unusable. For this reason it is crucial for viable biohybrid implants to achieve high degrees of growth directionality. Likewise, more sophisticated models focusing on functional aspects of the peripheral nervous system (PNS) may benefit from directional in vitro models. PNS circuits generally show a pattern where sensory-, or motor axons converge to form a nerve that eventually diverges again in the target location. Building an in vitro platform resembling this architecture would be extremely useful for studying neuropathy, traumatic nerve injury, tissue reinnervation and [neurapraxia, axonotmesis, neurotmesis ?], and the effects of nerve stretching. The canonical design of the biohybrid implant where multiple RGC source nodes converge into a common output channel replicates this motif.

The challenge of achieving directional in vitro networks is often reduced to imposing axonal or dendritic growth constraints once the neurons are seeded. Although it is conceivable that initially randomly connected neural networks develop directional connections solely by an electrically imposed activity pattern (Markram et al. 1997), this approach has so far been to no avail. Therefore, various in vivo inspired approaches have been taken to instead induce control on axonal outgrowth. Axon guidance mechanisms in vivo rely, broadly speaking, on two categories of cues: mechanical and chemical ones (Weiss 1941, Goodman et al. 1984). Chemical cues have been employed for guidance by integrating substrate surface modifications favoring certain growth paths. Although many attempts are limited to micro patterning with PDL falling short of the highly complex chemical micro environment observed in vivo, still, a notable degree of axonal growth control is achieved (Yamamoto et al. 2016). While chemical guidance remains a promising direction for engineering defined neural networks in the future, mechanical guidance has shown more promising results at larger network scales (Forró et al. 2018).

The idea of utilizing mechanical growth guidance in vitro is largely based on advances in microfluidics for neuroscience (Millet and Gillette 2012, Neto et al. 2016). These platforms are commonly fabricated from Polydimethylsiloxane (PDMS), a polymer that can be molded at high resolution using soft lithography, while also exhibiting acceptable biocompatibility properties (Millet et al. 2007). 3D mechanical guidance principles are based on the inertia of growing axons, e.g. the inability to grow in sharp turns, and the tendency of axons to attach to edges (Francisco et al. 2007). These two findings are the basis of

numerous PDMS design motifs proposed in the literature to achieve directional growth through PDMS micro structures: barbed-, and narrowing channels, (Feber et al. 2015, Peyrin et al. 2011,) redirecting hooks and consecutive arches (Pirlo et al. 2011, Na et al. 2017, Renault et al. 2016, Holloway et al. 2019), and diode-like triangles (Gladkov et al. 2017, Isomura et al. 2015). So far, the most competitive multi node directional networks are based on a relatively simple motif, where axons detachment from sharp radii prevents growth in the undesired direction (Forró et al. 2018).

While Forró et al. 2018 presented respectable results for four-node-networks, the nerve model system and surely the biohybrid implant require an order of magnitude more nodes, while also deviating from the rather simple one-to-one connectivity scheme. In this work we present a high resolution screen on the growth directionality in twenty many-to-one PDMS designs. . . .

2.4 Multiple object tracking

In this work, we employ a custom build, machine learning-based growth cone tracking model to screen PDMS micro structures for directional growth. Previous work has relied on screening network directionality electrophysiologically (Forró et al. 2018, Isomura et al. 2015, Feber et al. 2015), through calcium indicators (Na et al. 2017), manual-, or segmentation based axon counting (Pirlo et al. 2011, Forró et al. 2018) and by calculating fluoresce intensity ratios (Renault et al. 2016, Na et al. 2017). Due to the general geometrical complexity and the multitude of junctions within our micro structure designs, previously employed anatomically-based screening methods did not meet our requirements. Alternatively, functional screening methods can offer high resolution, yet they are often limited to low experimental throughput. For those reasons, we resorted to tracking growth cones during the initial outgrowth phase, yielding a high resolution, anatomically-based estimation of directionality.

The problem of multiple object tracking (MOT) consists of identifying objects and linking their identities over multiple video frames, either offline with the entire sequence available, or online/ causally where future frames are not observed. Extensions of this include the classification and segmentation of identified objects. With notable exception Braso and Leal-Taixe 2019, this problem has been divided into object detection and object association. Since the seminal paper by Krizhevsky, Sutskever, and Hinton 2017 introducing the concept on learned convolution kernels, object detection has been increasingly dominated by machine learning based detectors. While the architecture of an image classifier is straight forward, mapping from the image pixel map to the number of classes, object detection deals with an unknown number of instances within an image, making it unclear what the network output shape should be. The first solution to this problem was the recurrent convolution neural network (R-CNN) architecture by (citation), implementing the recurrent classification of small image regions (for improved versions see (Girshick 2015, Ren et al. 2015)). The inherently low inference speed in these architectures was addressed by the *you only look once* (YOLO) architecture by dropping the recursive aspect completely (Redmon et al. 2015, Redmon and Farhadi 2018, Long et al. 2020). The ensuing step of data association has been dominated by non machine learning based methods (Bewley et al. 2016, Kuhn 1955, Wang, Wang, and Yu 2019), although deep learning alternatives have recently been proposed as well (Wojke, Bewley,

and Paulus 2017, Yoon et al. 2019).

In the biological microscopy literature, the above is often found under the term *particle tracking*, indicating the focus on small objects such as cells, organelles, or proteins (Tsai et al. 2019, Anjum and Gurari 2020, Welshans and Bassell 2011). Although the general problem matches the outline above, tracking of biological objects, including growth cones, involves a specific set of additional problems. Concretely, the setup used for screening PDMS micro structures imposed the following challenges. (i) Objects of interest, i.e. growth cones are often extremely small, thus conventional CNN architectures based on hierarchical feature extraction of larger objects are not suitable. (ii) Microscopy images are taken at very high resolution, raising computational considerations. (iii) Inter frame intervals are long, here around 30 minutes, (iv) Growth cone appearance is highly variant; growth cones can overlap and collapse abruptly. (v) No labelled dataset exists, and widely available pretrained models generalize poorly. Our tracking implementation is build on established methods with modifications addressing the points i-v. For more details see methods 3.2.5.

3 Methods and Materials

3.1 Experimental procedures

3.1.1 Dish preparation

First, WillCo glass dishes (\varnothing 30 mm, WillCO Wells) were rinsed with acetone, isopropanol and ultra pure Water (Millipore Milli-Q System, 18M Ω), then dried with a nitrogen gun. Next, double sided adhesive (DSA) rings were used to attach WillCo glass dishes to polystyrene dish frames. The assembled dishes were placed in a larger plastic dish with tape stripes preventing surface adhesion between dishes.

3.1.2 Poly-D-Lysine & laminin coating

The assembled glass dishes were coated using 1 ml Poly-D-Lysine (PDL) solution, incubating for 1-2 hours at room temperature. The solution was prepared using 1 ml of thawed up PDL stock (P7280, Sigma-Aldrich), and 8 ml of phosphate buffered saline (PBS) (10010015, Gibco, Thermo Fisher Scientific, Switzerland). After incubation, the PDL solution was removed and the dishes were washed 2 times with PBS, and once with deionized (DI) water.

Subsequent to PDL application, dishes were coated with 10 μ g/ml laminin. This solution was prepared by slowly thawing 50 μ l aliquots on ice, then adding 5 ml of NeurobasalTM plus (A3582901, Gibco). Between 300-800 μ l laminin solution was applied to cover the whole surface of the glass dish. After 24h incubation at 37 °C, laminin solution was removed and the dishes were washed 1 time with PBS, and 2 times with DI water.

| Component | Volume [ml] | Stored at [°C] |
|---|-------------|----------------|
| Neurobasal Plus (Gibco, A3582901) | 237.5 | 4 |
| DMEM (Gibco 11960) | 237.5 | 4 |
| Glutamax | 5 | 4 |
| Sodium Pyruvate (100mM, Gibco 11360-070) | 5 | 4 |
| Antibiotic-Antimycotic (100x, Gibco 15240096) | 5 | -20 |
| N2 Supplement | 5 | -20 |
| B27+ (50x) | 10 | -20 |
| N21 Supplement (50x, R&D Systems AR008) | 10 | -20 |
| NAC Stock (5 mg/mL) | 0.5 | -20 |
| Forskolin Stock (4.2 mg/mL) | 0.5 | -20 |
| BDNF Stock (50 µg/mL, Preprotech 450-02) | 0.5 | -20 |
| CNTF Stock (10 µg/mL, Preprotech 450-13) | 0.5 | -80 |
| NGF 7S Stock (10 µg/mL, final 10 ng/mL) | 0.5 | -80 |
| GNDNF (10 ng/mL) | 0.5 | -20 |

Table 1: RGC medium composition. This medium was used throughout for culturing RGC neurons.

3.1.3 PDMS micro structure design, fabrication & mounting

PDMS micro structures were designed in a multi stage computer aided design (CAD) process. This was necessitated by the vast number of design motifs investigated in this study. Although not primarily intended for 2D CAD, Fusion360 (Autodesk, San Rafael, California) was used in the initial design stage. Fusion360 was chosen because of its powerful version control and design history system, enabling the natural integration of design variables into the CAD workflow. More concretely, specific elements in different PDMS designs were inserted as separate components such that they could be updated independently from the base designs; for example the commonly used 2-joint motif. Single PDMS designs were then exported as .dxf files by projecting extruded bodies to 2D sketches. Importantly, the projection link had to be deleted to export valid .dxf files. The single PDMS designs were imported to AutoCAD (Autodesk, San Rafael, California) to define fabrication mask layers and arrange designs on the wafer. Finally, the wafer design was exported as a .dxf file and imported from KLayout where the final .gds2 file was generated. The wafer and PDMS designs were fabricated by Wunderlichips (Switzerland) employing standard soft lithography (for details see Forró et al. 2018).

The PDMS membrane delivered by Wunderlichips was separated into independent PDMS structures on a laser cutter (Speedy300, Trotec, Switzerland) using 8 % power at 14 cm/s. Subsequently, the structures were thoroughly rinsed with 70 % ethanol. For a subset of experiments, a PDMS frame was laser cut from 5mm thick cured PDMS. Using uncured PDMS, it was attached on the micro structure to enclose the output channel area. After curing for 1h at 80°C, they were picked up with a pair of surgical forceps and slowly placed on the coated glass dishes (see above). Importantly, a thin film of DI water was put on the glass dishes to facilitate mounting without enclosed air bubbles. As the last dish preparation step, RGC medium (see composition in Table 1) was added and the dishes were desiccated for 30-60 minutes to remove air from the PDMS micro channels.

3.1.4 Retina dissection

Animal experiments were performed with highest of care maximizing animal welfare and following 3 R. The approval was obtained from Cantonal Veterinary Office Zurich, Switzerland under license –LICENSE–. E18 time-mated pregnant rats (Janvier Laboratories, France) were sacrificed and embryonic eyes were collected in hibernate on ice. Before retinal dissection, instruments were disinfected using 70% ethanol. Under a benchtop microscope (DFC420C with 4X magnification, Leica, Germany), eyeballs were pierced near the ciliary muscles using a sharp pair of forceps. This opening was carefully extended by inserting a second pair of forceps on which the sclera was subsequently striped off. Retinas were collected in hibernate on ice after gently removing the lens and minengees.

3.1.5 Spheroid creation

To create RGC spheroids, first, 500 μ l of AggreWellTM rinsing solution was added to the AggreWellTM 800 microwell plates. To ensure the absence of air bubbles in the microwells, the plate was centrifuged at 2000 g for 5 minutes or until no air bubbles were observed. Finally, the rinsing solution was washed away with Neurobasal medium and 1 ml of RGC medium was added to each of the micro wells.

For retinal dissociation, first, a solution was prepared by dissolving 50 mg BSA and 90.08 mg glucose in 50 ml of sterile PBS. 5 ml of this solution were vortexed with 2.5 mg Papain. After 30 minutes of incubation at room temperature, the Papain solution was filtered using a 0.2 μ m sterile filter and 5 μ l DNase were added. Retinas were dissociated by first incubating them for 15 minutes at 37 °C in 5 ml of this Papain solution. After 15 minutes, the Papain solution was carefully removed without disturbing the pallet. In three cycles, 5 ml of warmed Neurobasal medium were added, incubated for 3 minutes, then removed again. To suspend the retinas, 2 ml of RGC medium were added and repeatedly pipetted up and down using a pipette boy. After cell straining with a 40 μ m filter, the number of viable cells was determined using a Trypan Blue stain on a hemocytometer. To create spheroids of 3000 cells, the appropriate cell concentration to fill 300 micro wells was calculated and prepared. In order to obtain constant volumina across experiments, wells were filled up to 2 ml using RGC medium. Lastly, to color RGCs, 1 μ l of mRuby (scAAV-DJ/2-hSyn1-chl-mRuby3-SV40p(A)) or was added for adeno associated virus (AAV) mediated transduction. The AggreWellTM plate was then centrifuged at 100 g for 3 minutes to fill the microwells with cells. After confirming even cell distribution and expected spheroid sizes, the plate was placed in the incubator at 37 °C with 5% CO₂ for 16-20 hours.

3.1.6 Seeding PDMS micro structures

To remove the virus before seeding, spheroids were pipetted out of the AggreWellTM plate into a small petri dish and carefully washed in Neurobasal three times. Under the benchtop microscope, around 50 spheroids were pipetted from the petri dish into the prepared micro structure dish (see 3.1.3). They were then carefully placed in the appropriate location within the PDMS micro structures using a pair of micro scalpels. After 10 minutes of seeding, the culture was always put back in the incubator for 5 minutes. Once all seeding spots were filled, the culture was placed in the incubator at 37 °C with 5 % CO₂. Half the RGC medium was exchanged every 3-4 days.

3.1.7 Timelapse recording & image acquisition

Both timelapse,- and single images were recorded on an inverted confocal laser scanning microscope (CLSM) (FLUOVIEW FV3000, Olympus). Timelapse recordings were performed using a 20x objective, 800 μm pinhole, a gain of 580-600 V, and laser power of 0.8-1 %. The axonal growth in each of the approx. 40 PDMS micro structures was captured by 2 x 4, 1024x1024 tile scans, resulting in an optical resolution of 0.49 μm , and a pixel size of 0.62 μm . Absorption and emission spectra of fluorescent markers were set according to the manufacturers recommendations. To maintain cell viability throughout the recording, the integrated incubator chamber was setup to 37 °C with 5 % CO₂. Fast solid state storage media was used to prevent a frame rate bottleneck from an insufficiently fast network connection.

Single images were acquired under the same settings, except that a 10x objective was used. This resulted in an optical resolution of 0.88 μm and a pixel size of 1.24 μm .

3.2 Data analysis

3.2.1 Timelapse datasets

This work incorporates three PDMS micro structure timelapse recordings that were acquired at different timepoints. Accordingly, the data used in this work is based on three experiments, where each experiment was performed with 8-14 rat embryos (compare 3.1.4 for details). One of the three timelapses was solely obtained for generating model training data, thus the presented results are based on two experiments with a total of 16-28 biological replicates. A summary of timelapse datasets is given in Table 2.

We treat each half of a PDMS micro structures as independent samples, as all designs are strictly symmetric around the output channel. Given that the two experiments included each design in duplicate, a maximum of 8 samples per design were obtained. However, since fabrication failure within designs, bad tracking performance, and overly strong undergrowth led to discarding samples, few designs are limited to a sample size of $n = 4$.

| | Acquired | Setup | T [min] | n frames | Length [days] | Model usage |
|----------|----------|----------------------|---------|----------|---------------|-------------|
| Dataset1 | 20.12.20 | 1 designs | 40 | 37 | 1 | Training |
| Dataset2 | 27.08.21 | 2 designs, chamber | 31 | 210 | 4.5 | Training |
| Dataset3 | 27.10.21 | 18 designs, chamber | 31 | 210 | 4.5 | Inference |
| Dataset4 | 07.10.21 | 21 designs, stomachs | 32 | 242 | 5.4 | Inference |

Table 2: Overview of timelapse recording data. *n designs* refers to the number of unique PDMS micro structure designs composing the dataset. *Chamber* setups employed large thalamic tissue pieces enclosed by a PDMS frame for concentrated attraction cues (see 3.1.3 for details). *Stomach* setups omitted PDMS frames and instead seeded a thalamic spheroid in the target well (see Figure 3 for stomach illustration). T refers to the temporal period of the recording. White space between rows indicates different experiments.

3.2.2 Initial timelapse processing

The proprietary `.oir` files produced by the CLSM were converted to three dimensional `.tif` files using Python's `bioformats` package, which relies on a java virtual machine implemented within the `javabridge` package. Additionally, `.tif` frame sequences were rendered to `.mp4` video using `scikit-image` and `open-cv` (Suppl. Figure 1 A). These videos were used for initial evaluation of the timelapse, validating for example absence of undergrowth. The transmission channel of each PDMS micro structure timelapse was then loaded into napari, a python based n-dimensional image viewer (Sofroniew et al. 2021). Using `skimage.filters` to segment the micro channels in the PDMS designs, edge magnitude was detected with `prewitt()`, gaussian smoothing was performed with `gaussian()` ($\sigma = 1$), thresholding was done with `threshold_otsu()`, and finally, the segmentation was cleaned up using `skimage.morphology.binary_closing()` (diameter = 4) (Suppl. Figure 1 B). Subsequently, the segmentation of the PDMS micro channels was manually cleaned up, mainly using the bucket tool to fill areas enclosed by detected edges. To remove patches in the mask, the target point of the PDMS design was labelled and used as the origin to perform `skimage.segmentation.flood()`. As a last step, both the final output channel and the first 100 μm of the channels exiting the source wells were segmented and saved as binary masks (Suppl. Figure 1 C).

3.2.3 Axon growth cone labelling

The axon growth cone tracking model was trained using Dataset1, and Dataset2 which included timelapse recordings of three unique PDMS designs (compare Table 2). The labelling of these three image sequences was performed by one human expert using the napari image viewer (Suppl. Figure 2 A). The workflow for obtaining the four dimensional label of `FrameID - AxonID - X coordinates - Y coordinate` was as follows:

1. Load timelapse sequence.
2. Create empty set of axon identities.
3. Inspect short time slice of 3-6 frames for distinct, coherently moving blob.
4. Identify axon identity by its growth cone.
5. Trace axon identify over adjacent frames until unidentifiable.

In the scenario where two separate growth cones converge forming a single observable growth cone, one of the two identities was arbitrarily chosen to be continued while the other one was terminated. Hence, the underlying number of axons for a given growth cone label may be larger than one. It should also be considered that there is some degree of uncertainty in the ground truth labels. Especially when the PDMS micro channels become largely filled, distinguishing between GFP-protein trafficking along existing axons versus new growth cones becomes challenging. The annotations here were consistently done more conservatively, weighting the avoidance of false positives higher than missing true positives. Following this conservative labelling methodology, an axon identity was only considered if it appeared over more than three frames. From three concatenated PDMS micro structure timelapses, 300 growth cones were identified over N=327 frames where the average axon identity lifetime was 24 frames. An overview of the identify lifetime is given in Suppl. Figure 2 B; four labelled example frames are shown in Suppl. Figure 3.

3.2.4 Timelapse data preprocessing

The CLSM 12bit gray scale intensity values saved as 16bit unsigned integers were first converted to a scale of 0 to 1 using `skimage.util.img_as_float()`. For image sequences that had an offset in the intensity profile, this offset was subtracted such that the minimal intensity was always 0. Next, the segmentation of the micro channels was used to mask the image sequence (see Suppl. Figure 1 C for example mask). The resulting initial distribution of intensity values for both training and inference data is shown in (Figure 1 A top left). In the next step, intensity values below threshold = 0.00083 were clipped and set to 0 (Figure 1 A top right). Next, the intensity profile I_{in} was stretched using `skimage.exposure.adjust_log()` function with a gain $g = 1$ which transformed the distribution according to formula 1 (Figure 1 A bottom left).

$$I_{out} = g * \log(1 + I_{in}) \quad (1)$$

Finally, the intensity distribution was divided by the global standard deviation across the entire training image sequence, ensuring unit variance in the model input data (Figure 1 A bottom right). Both frame-wise, and mean-related standardizations were omitted since their application resulted in decreased detection performance. The intensity distributions from train- and inference data do not overlap in Figure 1 A because the sparsity differs vastly across frames. Train intensity values do not increase from t_0 to t_N because t_N corresponds to a different timelapse video (Dataset2) which is more sparse than t_0 (Dataset1).

3.2.5 Growth cone detection model

3.2.5.1 Temporal context frames

The growth cone detection model implemented in PyTorch follows the general approach of YOLO (You Only Look Once) (Redmon et al. 2015) where the detections are obtained by a single pass through the network (Figure 1 B). The first aspect in which it deviates from the original is that instead of inputting an RGB image, the network receives a temporal stack of five gray scale images. Concretely, to detect growth cones at frame t_0 , frame $t_{-2}, t_{-1}, t_0, t_1, t_2$ are fed into the network. This architecture aims to imitate the strategy of human labelling: by inspecting single frames, growth cone identification is highly uncertain; only when scanning sequences of frames, coherently moving blobs of particular shape and dynamics can be linked to growth cones and thus an axon identity. To always provide full temporal context, frame t_0, t_1, t_{N-1}, t_N were omitted from detecting growth cones in the image sequence. Computing the motion between frames manually by subtraction yielded decreased detection performance over the implicit approach of passing temporal context frames. An illustration of the motion computation is shown in Figure 1 C.

3.2.5.2 Tiling

Each yellow block in Figure 1 B represents a sequence of 2D-convolution, batch normalization (Ioffe and Szegedy 2015), and Leaky ReLU (Maas, Hannun, and Ng 2013). Orange layers stand for maximum pooling operations. As performing detection on the original resolution of 3868 x 1972 was computationally intractable, the timelapse frames were split into 512 x 512 tiles (see Figure 1 C and grid in Suppl. Figure 3). The CNN computes a convolutional feature map of 16 x 16 x 160, thus a single *feature pixel* represents a region

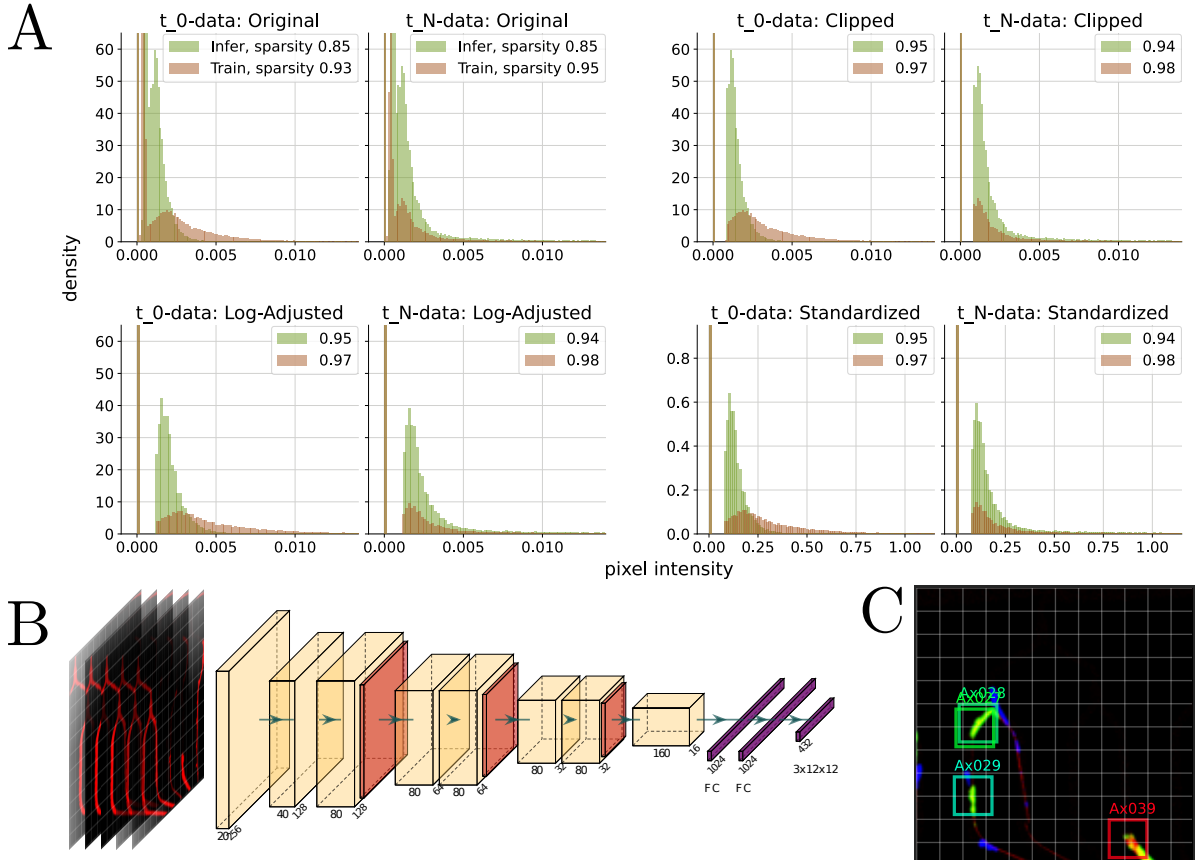


Figure 1: Growth cone detection model overview. **A** Pixel intensity distribution of training-, and inference data at t_0 and t_N over three major preprocessing steps. The two plots top left show the initial pixel intensity distributions, top right after clipping, bottom left after log adjusting, and bottom right after standardization. Histograms on the left were obtained from sampling 10^6 pixel values from the first frame, histograms on the right from the last respective frame. The inference data to produce the histograms (brown) was taken from a representative image sequence from Dataset3 (see Table 2). The number in the legend indicates the proportion of image values equal to zero (sparsity). Note that outlier intensity values are not shown. **B** CNN architecture. Each yellow block in represents a sequence of 2D-convolution, batch normalization (Ioffe and Szegedy 2015), and Leaky ReLU (Maas, Hannun, and Ng 2013). Orange layers stand for maximum pooling operations. FC stands for fully connected layers. **C** Example tile illustrating the YOLO label format. Each grid box can be predicted to contain a growth cone. In this example, 4 of 12 x 12 grid boxes are positive. Green colors in the tile represent positive motion (pixel intensity increased from frame t_0 to t_1), blue represents negative motion. Grid box size = 26 μm .

of $\frac{512}{16} = 32$ pixels in the original 512 x 512 input image. The CNN output resolution was a relevant consideration for its architecture, as the detection objects of interest are small and potentially locally clustered (using microscopy settings described in ??, growth cones are between 4-26 pixels). If the same CNN feature output resolution was to be achieved using original timelapse frames, the CNN output would be of shape of $\frac{3868}{32} \times \frac{1972}{32} \times 160 \approx 120 \times 61 \times 160$. Storing the weights between this high-resolution CNN feature map and the first fully connected layer exceeded GPU memory. An additional computational benefit is achieved by skipping empty tiles. From visual inspection, the discontinuities between tiles did not seem to result in decreased detection performance for growth cones near the tile edges.

3.2.5.3 Detection output format

Following the general YOLO label format, the network is trained to find a mapping from a single tile CNN feature map to a 12 x 12 x 3 array. Here, the first two dimensions represent a grid of the input tile, the last dimension refers to the confidence of the respective grid box containing a growth cone, and X-, Y grid box coordinates referring to the relative location of a growth cone within the box (Figure 1 C). This representation results in the limitation, that only one growth cone can be detected per grid box. As the example in Figure 1 C shows, close growth cones may still be detected as two separate identities if their centers are located in different grid boxes. In the worst case scenario, the spatial detection resolution of multiple growth cones is limited by the grid box size which is equal to $\frac{512}{12} = 43$ pixels or 26 μm . This resolution was sufficient for the application of our model as densely grouped growth cones were the exception.

To drop overlapping detections, non max suppression was applied to the final detection output according to (Bodla et al. 2017) using a minimum euclidean distance of 23 pixels.

3.2.5.4 Training procedure

The training data was split into 287 train frames (0.87), and 40 (0.13) consecutive test frames which spanned two different PDMS micro structures. The final model used for inference was trained on the entire dataset. Using translation, rotation, horizontal and vertical flipping as data augmentation, the model was trained up to convergence for 1000 epochs (Figure 2 A). The loss function below (2) is a slight modification from the original.

$$\lambda_{anchor} \sum_{i=0}^{S^2} \sum_{j=0}^B \mathbb{I}_{ij}^{obj} [(x_i - \hat{x}_i)^2 + (y_i - \hat{y}_i)^2] + \lambda_{obj} \sum_{i=0}^{S^2} \sum_{j=0}^B \mathbb{I}_{ij}^{obj} (c_i - \hat{c}_i)^2 + \lambda_{noobj} \sum_{i=0}^{S^2} \sum_{j=0}^B \mathbb{I}_{ij}^{noobj} (c_i - \hat{c}_i)^2 \quad (2)$$

where $S = 12$ is the number of tiles, $B = 1$ is the number of detections per grid box, \mathbb{I}_{ij}^{obj} equals to 1 if a growth cone exists, 0 otherwise, \mathbb{I}_{ij}^{noobj} equals to 0 if a growth cone exists, 1 otherwise, c_i refers to the confidence that an object exists in the grid box, and x_i, y_i represent the grid box coordinates. $\hat{\cdot}$ stands for the ground truth label. The loss terms for predicting coordinates, object presence, and object absence are weighted according to $\lambda_{anchor} = 45$, $\lambda_{obj} = 54.25$, and $\lambda_{noobj} = 0.75$ respectively. The balancing of those terms is based on the proportion of positive grid boxes which is $\approx 0.7\%$. The initial learning rate was set to 0.0005 and decayed with a rate given in formula 3.

$$\gamma = e^{-\frac{1}{10}\sqrt{x}} \quad (3)$$

where γ is multiplied with the original learning rate, and x refers to the current epoch. Pytorch's Adam optimizer (Kingma and Ba 2014) was used for fitting the model with $\beta_1 = 0.9$, $\beta_2 = 0.999$.

3.2.5.5 Data association

The implemented growth cone tracking model follows a classical object tracking paradigm of splitting the problem into object detection and identity association. For this second step, the detections produced by the YOLO-like architecture need to be classified into unique growth cone identities that live over several video frames. In this work, identity assignment is framed as a graph problem where we seek minimum cost flow solutions (Wang, Wang, and Yu 2019). At a high level, nodes represent detections at particular frames, and edges represent identity associations between them (see illustration in Figure 2 E). Each detection confidence is also represented as an edge, which elegantly incorporates the detection model uncertainty into forming identity trajectories through the graph and avoids the setting of explicit detection confidence thresholds. At the basis of associating detections between frames is the cost we assign between them. This cost can be interpreted as the likelihood the two detections correspond to the same growth cone identity. In contrast to other domains where visual similarity is highly relevant, because of the large morphological variance, the edge costs here are completely based on the spatial distance between detections. Specifically, the A* distances (Hart, Nilsson, and Raphael 1968) between detections computed on the segmented PDMS micro channel mask using a custom C++ implementation. This cost considers the constraint, that growth cones can only translocate within the micro channels and are limited in outgrowth speed. Solving the graph optimization problem includes the constraint, that a node can only receive and emit a single edge, or in other words, a node can only represent a single identity. As shown by Wang, Wang, and Yu 2019, the graph can be solved optimally and efficiently using integer linear programming. The implementation here is based on the open-source package `libmot`, using the build-in `MinCostFlowTracker`. The optimal hyperparameters listed and explained in table 3 were identified with a grid-search algorithm on test data (see Figure 2 D).

3.2.6 Directionality inference from tracking

Using the growth cone trajectories obtained from the model, the degree of directional growth through the PDMS micro structures can be inferred. Analogous to the identity association cost employed for formulating the graph, directionality inference also relies on computing A* paths on the micro channel segmentation mask. For each detection that composes the growth cone trajectory, we compute the shortest distance to a human-labelled target point located in the output channel (see Suppl. Figure 1 C). Our PDMS designs have the property, that the shortest path towards this point is precisely the desired growth path. More intuitively, the desired growth path towards the output channel has no detours. Thus, we can employ the A*-shortest path towards the output channel as a proxy for confirming the correct growth direction through the micro channels. Concretely, a correctly growing axon should exhibit constantly decreasing A* distances towards the output channel. Conversely, any increase in distance indicates growth in the undesired direction.

A variety of metrics were considered for evaluating the degree of directional growth

| | | |
|--------------------------|---------------------------|----------------------|
| Edge cost threshold | Entry-exit cost | Miss rate |
| 0.7 | 2 | 0.6 |
| Maximum number of misses | Minimum network flow | Maximum network flow |
| 1 | 5 | 450 |
| Visual similarity weight | Confidence capping method | |
| 0 | <i>scale</i> | |

Table 3: Minimum cost flow hyperparameters. The edge cost threshold determines if an edge is pruned or kept, the entry-exit cost defines the cost of creating and terminating identities, the maximum number of misses indicates for how many frames an identity can be not detected, but still not terminated, the miss rate determines how much cost is incurred from missing detections (low means high cost), minimum and maximum network flow gives the minimum and maximum number of identities over all frames, visual similarity weight determines the degree to which visual similarity between detections contributes to the cost, and finally the confidence capping method sets the behavior for confidence values above 1, where *scale* means normalize to maximum confidence.

through PDMS micro structures. Δ distance-to-output channel of each axon provides a large sample size, but axon track length is not the most direct metric of interest. To circumvent the bias of long axon tracks, we count the number of correctly,- and incorrectly growing axons, as the basic property of growth direction is more relevant than the overall covered distance. However, since this counting overvalues slow forward growth with little convergence to the final target location, we also analyse the number of axons reaching a neighbour, and the output channel, respectively. Preferably, we would rely solely on this metric, however, with the limited timelapse duration of around 5 days, many structures exhibit a very low number of axons reaching target and neighbours which reduces the sample size significantly. For this reason, this metric was only employed for qualitative measures. To obtain a final metric incorporating both forward convergence and backwards avoidance, we compute the smoothed directionality ratio δ of the two axon counts (Equation 4).

$$\delta = \frac{n_{target} + 1}{n_{neighbor} + 1} \quad (4)$$

where n_{target} and $n_{neighbor}$ refer to the number of axons reaching the output channel and a neighbour, respectively. One is added to both quantities to first, avoid discarding samples with no cross-growth, and second to lower the weights of small axon numbers. Intuitively speaking, the addition becomes negligible for large values, while reducing fold-differences of small, and thus potentially more uncertain counts. Alternative methods, for example normalizing to the sum of the two counts elicited less distinct differences between groups.

4 Results

4.1 Tracking performance

The presented model splits the tracking problem into growth cone detection and identity association. A representative example of detections is shown in Figure 2 B. Given the temporal stack of five image tiles, the detection model accurately identifies growth cones in PDMS micro structure timelapse frames. False positive detections made by the model are often ambiguous image regions that may be interpreted as positives under less conservative ground truth labelling. On the test set, the detector reaches a precision of 0.73, and recall of 0.79. F1 score at a confidence threshold of 0.79 is 0.76 (Figure 2 C). A both deeper and wider CNN architecture did show decreased performance. The ensuing step of identity association was performed in a graph framework optimizing for minimum cost flow solutions. Matching detection performance in tracking is challenging as in addition to detection, identity switches, object occlusions, and suitable identity creation-, and termination need to be considered. Using the multiple object tracking benchmarks proposed in ??, our tracker achieves identity precision, recall and F1 score of 0.73, 0.68, 0.71, respectively, which is a reasonably small drop from detection performance (Figure 2 D). The commonly used MOTA (multiple object tracking accuracy) metric which considers the number of false positives, false negatives (including identity), and identity switches normalized to the number of ground truth labels was 0.61. A more intuitive measure of tracking performance is visualized by the top bar in Figure 2 D, indicating the proportion of growth cones mostly tracked (0.57), partially tracked (0.23), and mostly lost (0.2).

Although not utilized for our application of the tracking model, axons can be reconstructed from the growth cone track, assuming that outgrowth followed the shortest path between detections.

4.2 Micro structure designs

The tracking model described above was used for evaluating a set of 21 PDMS micro structures designed for directing axon growth from multiple source regions towards a common target. These designs are the result of unpublished previous work extensively described in supplementary information 1. In short, the 21 designs test a set of presumably relevant variables that yield directional axonal growth, including different types of 2-joints, joint placements and joint frequencies. Figure 3 illustrates the specific features implemented in the different designs. Design 05 on the right exemplifies the general PDMS architecture composed of four source wells, the convergence lane, the higher output channel with added diffusion wells and finally a target stomach (Forró et al. 2018).

4.3 Between dataset variance

The translocation of RGC growth cones was tracked over a period of 4 days to infer the degree of directional growth through new PDMS micro structure designs. The directionality was evaluated based on the A* distance-to-output channel over time (see Methods 3.2.6). Figure 4 A shows this inference of directionality from output channel distances for tracking axons in design 5. Axons that grow towards the output channel exhibit smaller distances over time, thus the Δ distance towards the output channel is negative for directionally growing axons. These distances form the basis of subsequent analysis steps.

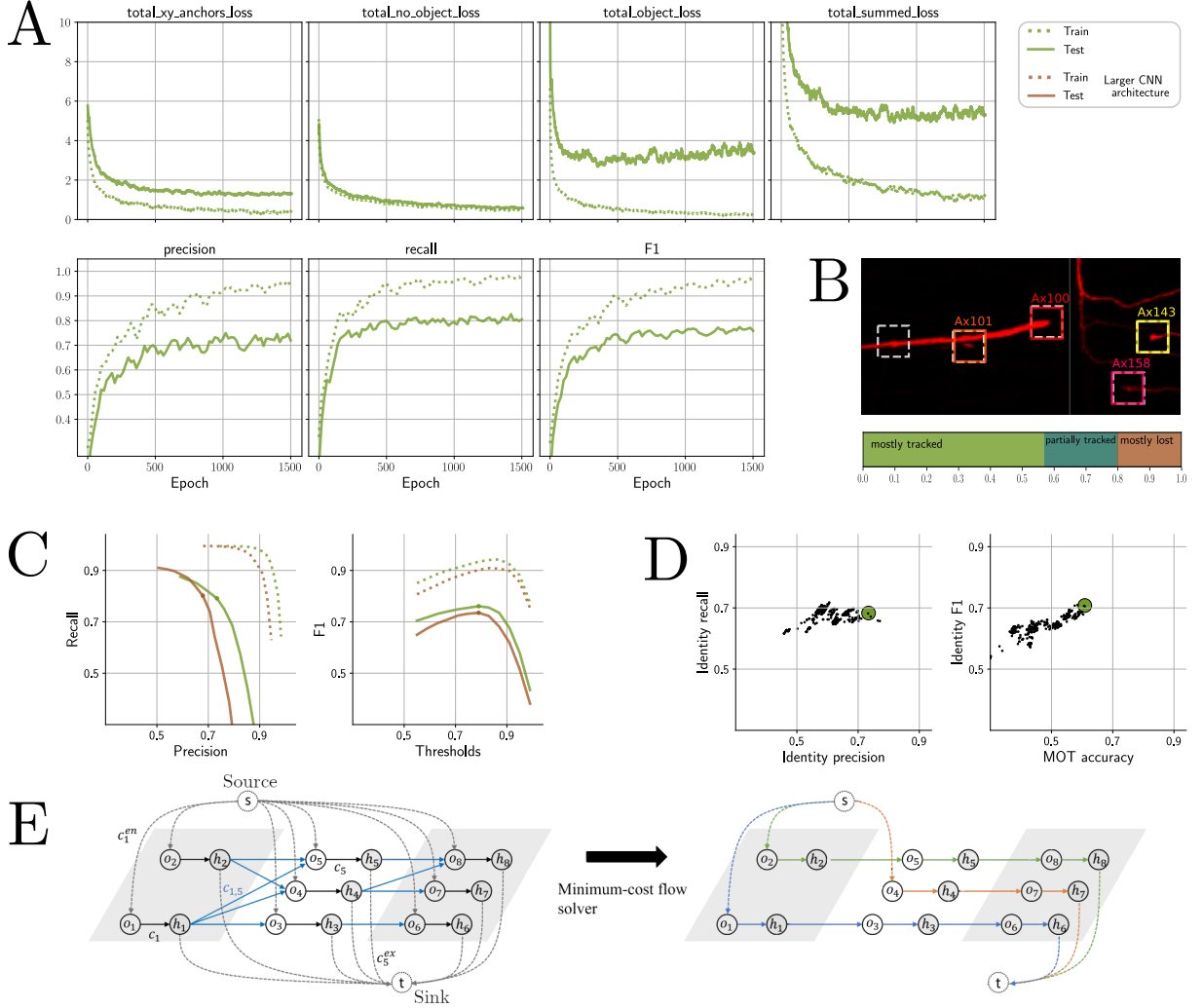


Figure 2: Growth cone tracking model performance. **A** Loss and performance over 1500 training epochs. Dotted line refers to train set, solid line to test. The plotted loss was smoothed with an exponentially decaying kernel over 25 epochs, precision, recall, and F1 over 60 epochs. **B** Representative growth cone detection example. Dashed boxes are predicted, colored ones are ground truth. Scale bar = 90 μm . **C** Detection performance. The maximum F1 score for varying confidence thresholds on test set is indicated by the dot. The brown line shows performance for a model with wider and deeper architecture. Legend in A applies. **D** Model growth cone tracking performance. Identity precision and recall incorporate classification of correct identity. Each black dot represents the performance using one set of hyperparameters, the green dot represents the highest scoring set (see Table 3) where identity F1 was 0.71, MOT accuracy 0.61. MOT accuracy measures the number of false positives, false negatives, and identity switches normalized to the number of ground truth labels. The top bar visualizes the proportion of growth cones that were mostly tracked (green, >80% identity lifetime tracked), mostly lost (brown, <20%), and partially tracked (dark green, between 20-80%). **E** Minimum cost flow optimization illustration adopted from (Wang, Wang, and Yu 2019). Frames are illustrated in gray and white background, detections within a frame are represented by a pre- (o_i), and post (h_i) node. Blue edges on the left represent costs between detections in adjacent frames. Coloured edges on the right indicate identity associations after solving the graph.

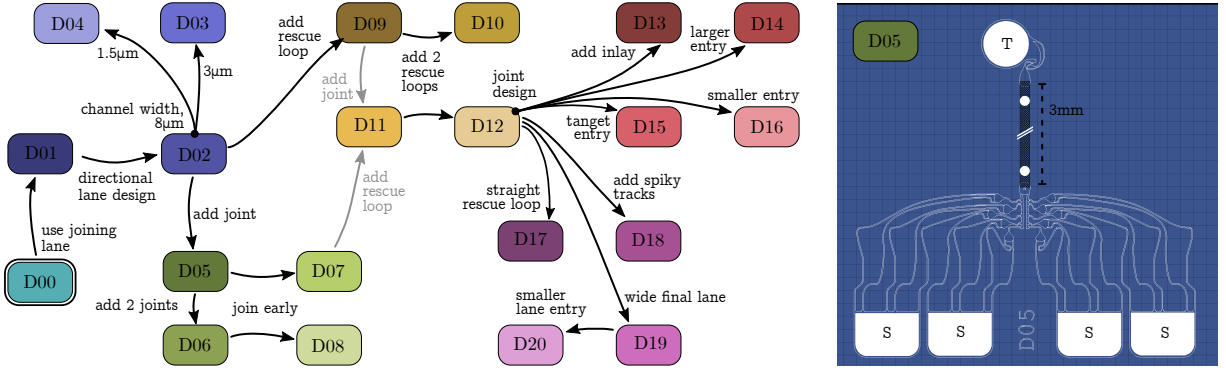


Figure 3: PDMS micro structure designs. The left illustration provides an overview of the 20 modelled micro structures including their distinguishing design features. Starting from design 0 (D00), the arrows can be interpreted as an implemented design change. For example, D05 and D06 differ specifically in the number of 2-joints. On the right, the D05 design is shown as an example. Filled white regions are openings, white lines indicate 6 μm high channels, the black region represents the 75 μm high output channel (note discontinuity for illustrative reason). RGC spheroids are seeded in the source wells (S), the thalamic attractor is placed in the target well (T). Grid dimension 100 μm .

Tracking was performed on two datasets obtained from experiments with slightly differing setups. While Dataset4 was acquired using thalamus spheroids placed in stomachs (see Figure 3 right), Dataset3 used free floating thalamic tissue pieces enclosed by PDMS frames to locally increase attractor concentration. Dataset3 and 4 exhibit a collection of significant differences. Figure 4 B highlights the variation of growth directionality between the two. During the initial outgrowth phase Δ distances collectively decrease for all designs by 300 μm in both datasets. Albeit with increasing variance, this average distance is kept throughout, indicating a dominance of non-moving growth cones. While the averages are comparable, the variance of directionality differs vastly between Dataset3 and 4. In contrast to Dataset3, Dataset4 shows only marginal differences between designs, and the overall variance is smaller. This discrepancy is condensed in Figure 4 B (right) with the temporal dimension collapsed. To better identify differences in directionality between designs, subsequent analysis was conducted on the interval with maximum variance, DIV 3.5 to 6 (see dashed line).

4.4 Axonal viability across datasets & designs

PDMS micro structure designs primarily focus on achieving directional growth towards the output channel. While this metric is crucial, as with any metric, ignoring other relevant factors may result in poor overall performance. In our case, these other relevant factors are indicators of neural viability, including axonal outgrowth velocity, frequency of outgrowth, long-term survival and electrical transmission efficacy. Although screening all these factors along side directionality performance was out of scope for this work, the tracking of growth cones yielded insights into frequency and velocity of axonal outgrowth. Intuitively, the frequency of outgrowth is directly derived from the number of unique axon identities. The growth velocity in [$\frac{\mu\text{m}}{\text{day}}$] was determined from the slope of distance-to-output channel over time (Figure 4 A). This allowed for a further metric, namely the classification of stagnating axons. Here, we defined axons as stagnating if the standard deviation of growth velocity over the last 5h of detection was below 12 [$\frac{\mu\text{m}}{\text{day}}$]. In Figure 4

A (top) stagnating axons clearly appear as horizontal lines.

In accordance with the directionality discrepancy between datasets described above, the complementary metrics of outgrowth frequency, outgrowth velocity and stagnation frequency differ significantly between datasets (Figure 4 C,E,F). Figure 4 C illustrates the growth speed over time for both datasets. Initially, the growth velocity is approximately 1100 [$\frac{\mu\text{m}}{\text{day}}$] with high variance. While the average growth velocity and variance decline over time in Dataset4, Dataset3 maintains the high initial outgrowth velocity. As expected, the number of stagnating axons per PDMS micro structure is significantly higher in Dataset4 (Figure 4 F). Lastly, the outgrowth frequency is significantly lower in Dataset4 (Figure 4 E).

So far, we have only grouped the data by dataset. To reveal potential effects of different PDMS designs on the axonal viability metrics, the dataset may be split by design features, such as the channel width, the number of rescue loops, and the number of 2-joints. Figure 4 D shows the effect of these three features on axonal growth velocity. Especially the PDMS micro channel width has a highly significant effect. By almost completely eliminating stagnation (Figure 4 F), the designs 3 and 4 which implement 3 and 1.5 μm wide channels respectively exhibit approximately double the growth velocity compared to 8 μm designs. A smaller yet highly significant relationship was identified between the number of 2-joints and rescue loops. Omitting both of these elements yields significantly higher growth velocity. While the number of 2-joints seems qualitatively anti correlated with growth velocity ($0 > 1 > 3$), the number of rescue loops is not, as designs with one rescue loop show significantly faster growth compared to designs with zero loops. Similar to growth velocity, the number of 2-joints seems to have a negative effect on axonal outgrowth frequency (Figure 4 E). The effect of other design features on viability metrics is shown in Suppl. Figure 5, 6, and 7.

4.5 Directionality in PDMS designs

Tracking growth cones provides insights into interesting axonal growth properties and their dependance on design features. However, the primary intention of tracking was to identify PDMS micro structure designs that results in high directional growth from seeding wells to output channel. As shown in Figure 4 A, the directionality is evaluated based on the A* distance-to-output channel over time. A simple approach suitable for large effect sizes is to compare distributions of axon wise Δ distances (see Figure 4 B, right). This method favors long axon tracks, which is not of direct interest. Rather, the qualitative property of growing in the correct,- or incorrect direction is relevant (see circles in Figure 4 A). Figure 5 A summarizes those counts of axons for all 21 designs, normalized to the total number of observed axons. While none of the single comparisons pass statistical significance with Holm-Bonferroni correction, the factor *design* has a significant impact on backwards growth. Forward growth counts exceed backward growth across all designs since the initial outgrowth is strongly biased towards forward growth. With approximately 65 %, the highest median of forward growing axons is observed in design 4 implementing 1.5 μm wide channels. However, this strong forward bias comes at the cost of the relatively high backward growth of 25 %, which is also observed in design 3 using 3 μm wide channels. In contrast, design 8 implementing frequent, late merging shows nearly no backward growing axons paired with average forward growth. The de-

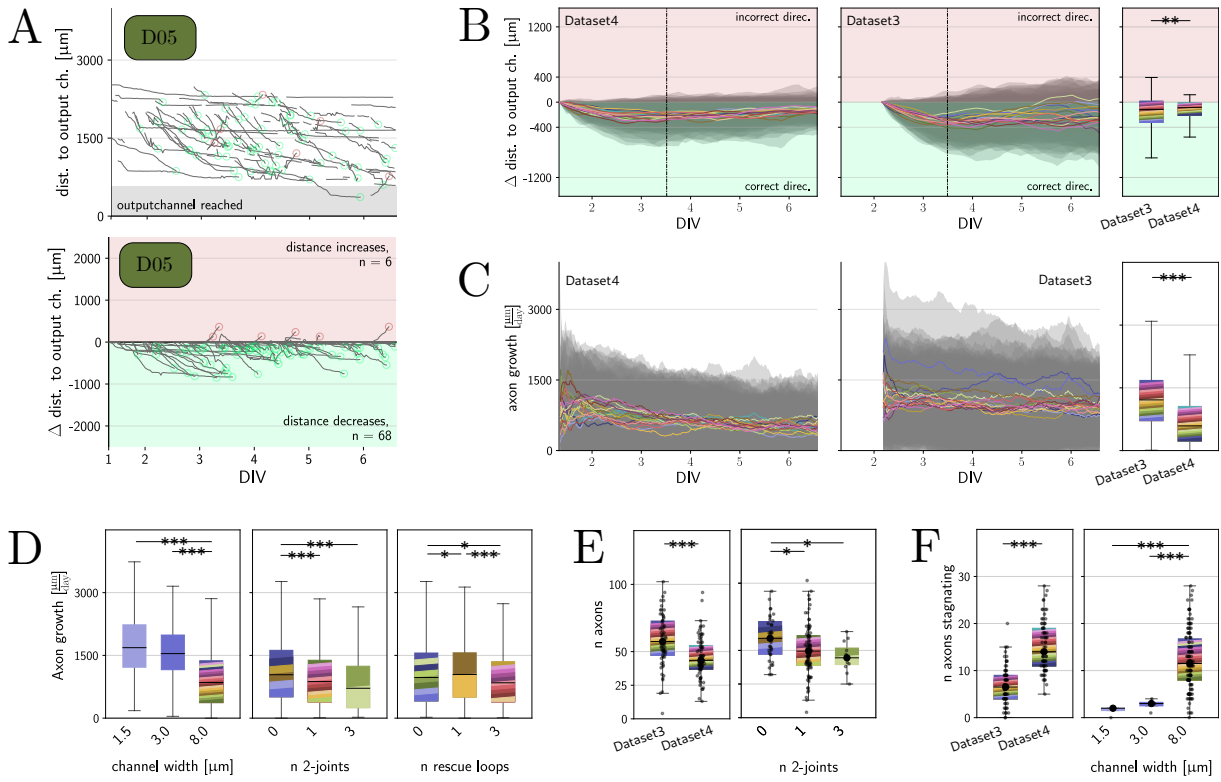


Figure 4: Between dataset variance and axonal viability. **A** Inferring directionality from distance-to-output channel exemplified in design 5. Each of the gray lines represents an axon identity, axons in the light gray region are inside the output channel. Subtracting the initial distance to the output channel yields the bottom plot. Green or red circles mark axons that grew at least 50 μm in the correct or incorrect direction, respectively. Count is given in corners. **B** Median growth directionality over time. Axon wise Δ directionality is computed by subtracting first- from last distance-to-output channel. Each colored line represents a design following the color code in Figure 3, gray regions indicate the standard deviation. **C** Axon growth velocity over time. **D** Axon growth velocity split by design feature. As for all following box plots, whiskers represent 1.5 x inter quartile range (IQR), and colors represent the 21 designs composing the distribution according to the color code in Figure 3. **E** Number of axons identified in one half of a PDMS micro structure. Single dots represent datapoints composing the distribution. **F** Number of stagnating axons identified in one half of a PDMS micro structure. Kruskal-Wallis test was used for non-parametric group comparisons, subsequently, the single comparisons were made using Mann-Whitney-U test with Holm-Bonferroni correction. * indicates $p < 0.05$, ** $p < 0.005$, and *** $p < 0.0005$. Applies for subsequent figures.

signs 12-20 which share the same general architecture but vary in specific motif designs collectively exhibit few (around 10 %) backwards growing axons. The forward growth distribution of design 18 using spiky tracts on unpreferred edges has the longest positive tail.

Grouping the data by design features instead of design can reveal more distinct trends. Figure 5 C and D summarize significant and non-significant effects, respectively. As mentioned before, smaller channel widths increase both forward,- and backward bias, however, only the backward effect is statistically significant. Another significant design feature is the number of 2-joints, or merging structures. Using one or three instead of none yields significantly lower backwards growth, whilst not affecting the forward bias. Conversely, forward bias is significantly impacted by the placement of 2-joints but does not have an

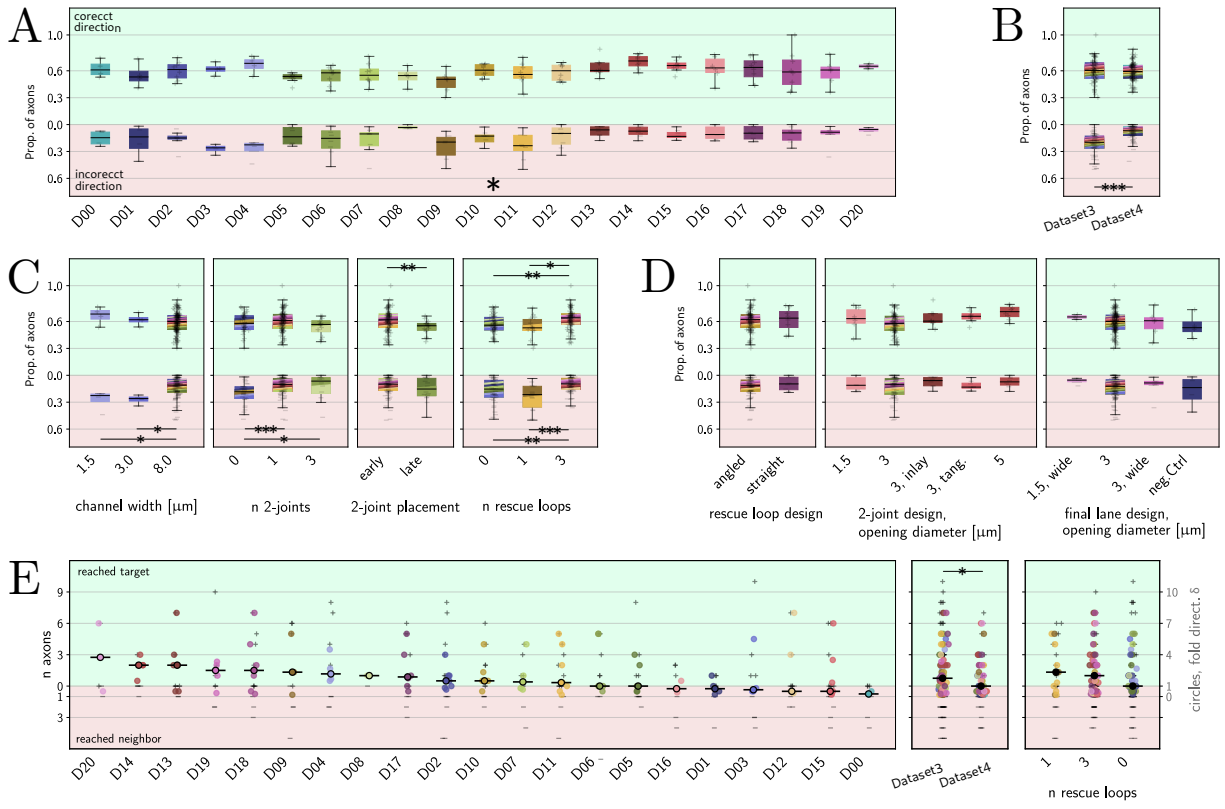


Figure 5: Directionality in PDMS designs. **A** Proportion of correctly,- and incorrectly growing axons in one half of a PDMS micro structure. Axons were counted if the Δ distance was above 50 μm . Faint + and - symbols compose the distributions, respectively. Applies for B, C and D as well. Star indicates that Kruskal-Wallis test evaluates the design as a significant factor for backwards growth, but single comparisons don't pass Mann-Whitney-U test with Holm-Bonferroni correction. **B** Number of correctly,- and incorrectly growing axons split by dataset. **C** Number of correctly,- and incorrectly growing axons split by significant features. **D** Number of correctly,- and incorrectly growing axons split by non-significant features. One other non-significant feature, the use of spiky tracts, is shown in Suppl. Figure 7. **E** PDMS micro structure designs ranked by δ fold directionality. Corresponding to the left y axis labels, + and - symbols represent the number of axons that reached the output channel or neighbor, n_{target} , $n_{neighbour}$, respectively. The colored circles represent the smoothed δ fold directionality computed from these two counts as formulated in equation 4, medians are indicated by horizontal lines. The axis labelling on the right applies for all circles.

effect on backwards growth counts. Joining channels early yields a significant increase in forward growth of approximately 10 %. Lastly, the number of rescue loops has an impact on both forward,- and backwards growth. Implementing three instead of one or none rescue loops prior to each 2-joint reduces the proportion of backwards growing axons. Forward bias was not only unaffected but significantly increased between three and fewer than three rescue loops. No significant effects were observed for angled versus straight rescue loop designs, spiky tracts, different variants of 2-joints and modifications to the final lane design (Figure 5 D).

As mentioned in the methods (3.2.6), focusing solely on growth direction counts may overestimate the performance of designs with low to medium forward convergence that do not reach critical joining areas. This is concretely observed when splitting by dataset

origin, as shown in Figure 5 B. Timelapse videos of Dataset4 show only few axons reaching 2-joints or final lane, thus backwards growth is significantly biased towards lower values. To compute an interpretable directionality metric that mitigates this directionality overestimation, we compute the ratio of axons reaching the output channel and axons reaching neighbors. Ranked by performance, both single axon counts and δ fold directionality are shown in Figure 5 E. Due to many samples showing neither target,- nor neighbor grown axons, δ measures were limited to fewer samples, resulting in almost no significant differences. Still, the metric provides valuable qualitative insights in comparison to directional counts in Figure 5 A. Consistent with good performance on growth direction counts, the five designs 20, 14, 13, 19, and 18 show δ fold directionality between almost 4 and 2.5. Hinting at the potential discrepancy between the two metrics, design 9 δ performance shows a tendency to be better than what relative growth direction counts indicate. δ below 1 is observed in design 0, 15, 12, 3, 1 and 16. These designs implementing no final lane, a final lane with,- and without directional promoting geometry, and 2-joints with medium-sized and tangent entries exhibit more axons reaching the neighbor than the output channel. The only significant differences in δ are observed when grouping by dataset. In sharp contrast to results in Figure 5 B, design measurements originating from Dataset4 show lower performance than those from Dataset3, highlighting the overestimation bias of counted growth direction clearly. In line with the observation in Figure 5 C, though not significant, the implementation of rescue loops tends to have a positive effect on the δ metric.

4.6 Axon guidance design primitives

We found that

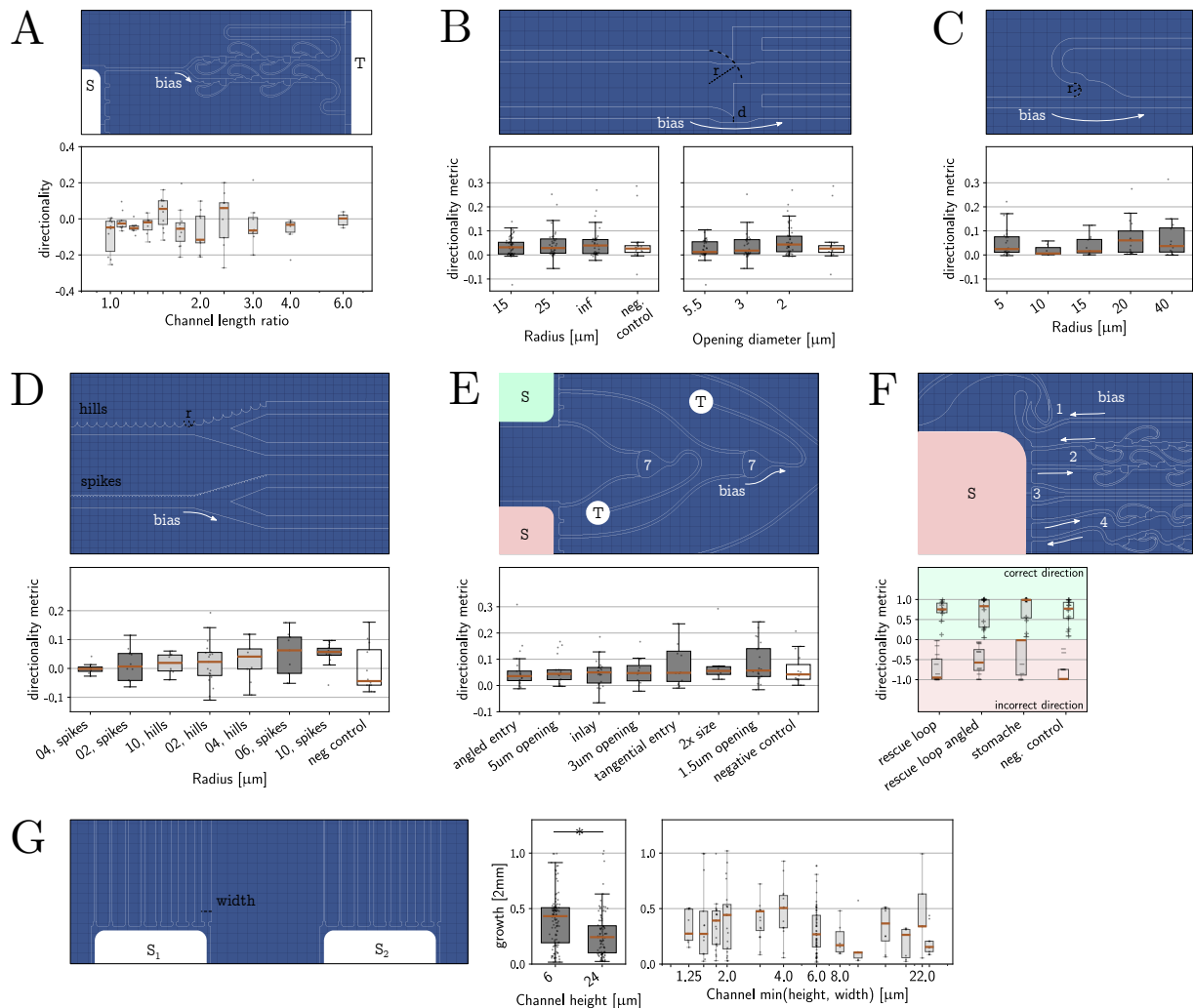


Figure 6: Screening of PDMS design primitives. **A** Effect of cue gradient on directional growth. The attractor cue gradient is produced by employing different distances towards the cue source (T) ...

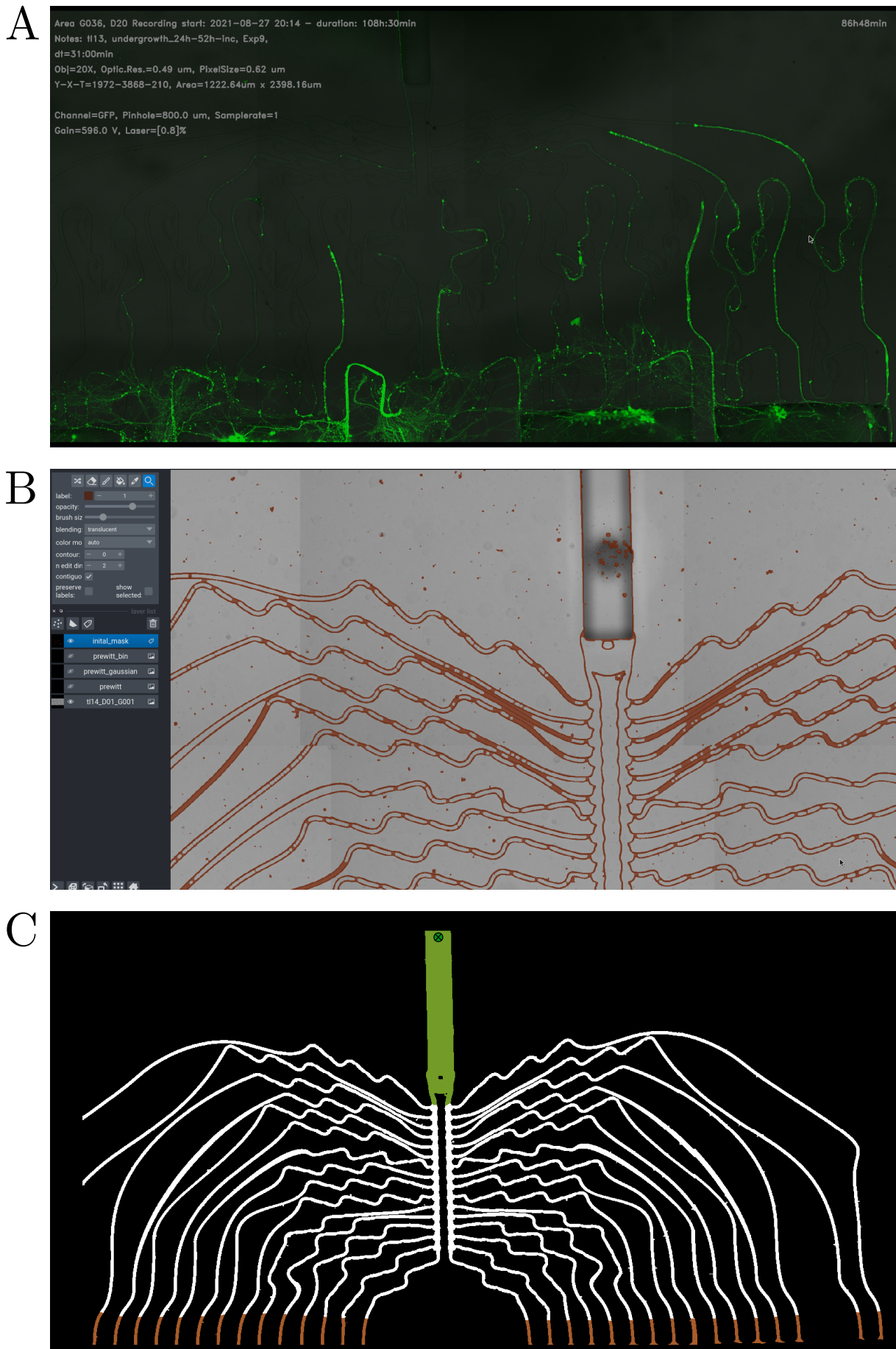
5 Discussion

5.1 Model architecture and generalization

treating numerical variables as categoric ones

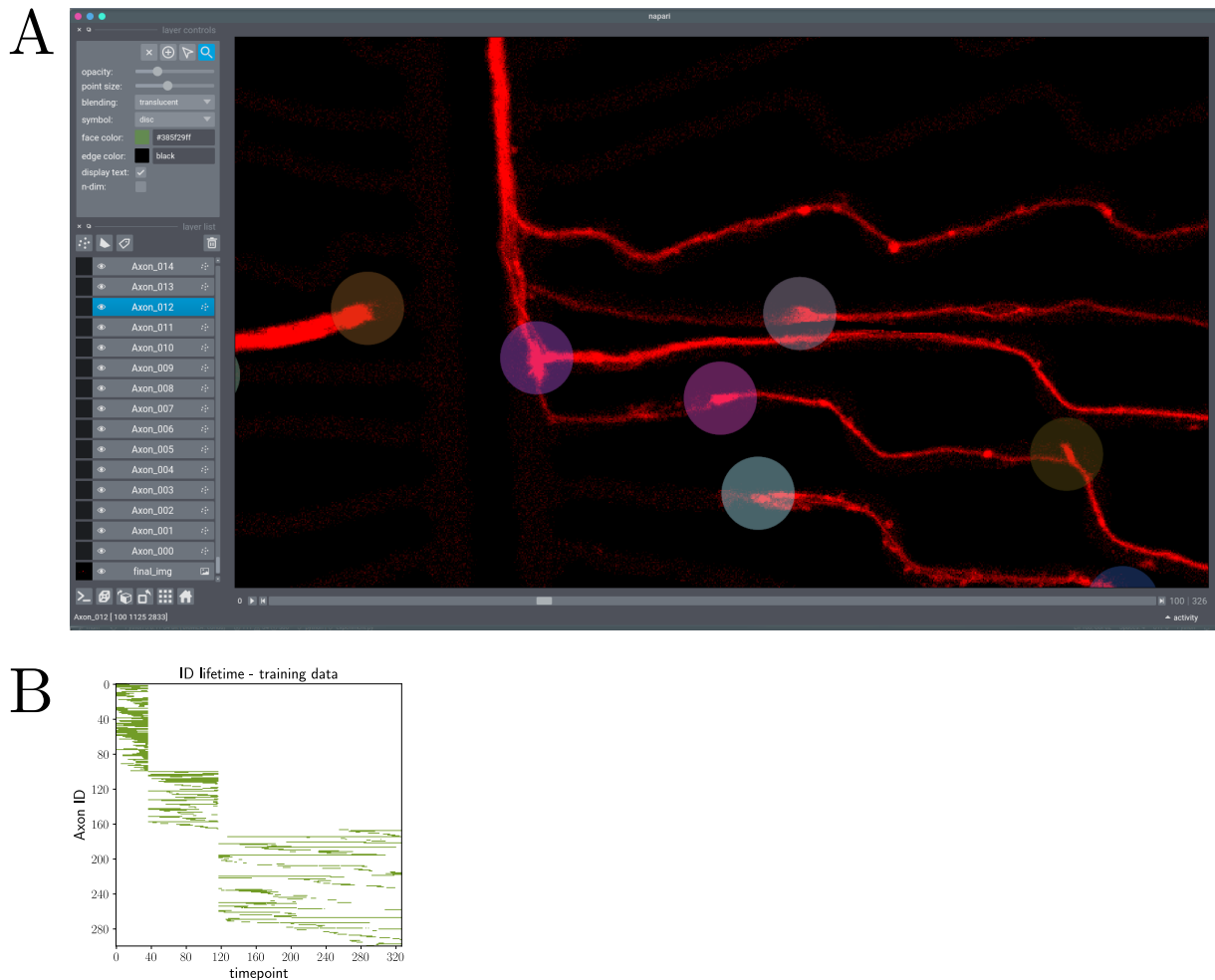
concern with viability results for n 2-joints: design 8 only in Dataset4, which has generally lower growth.

6 Supplementary Information

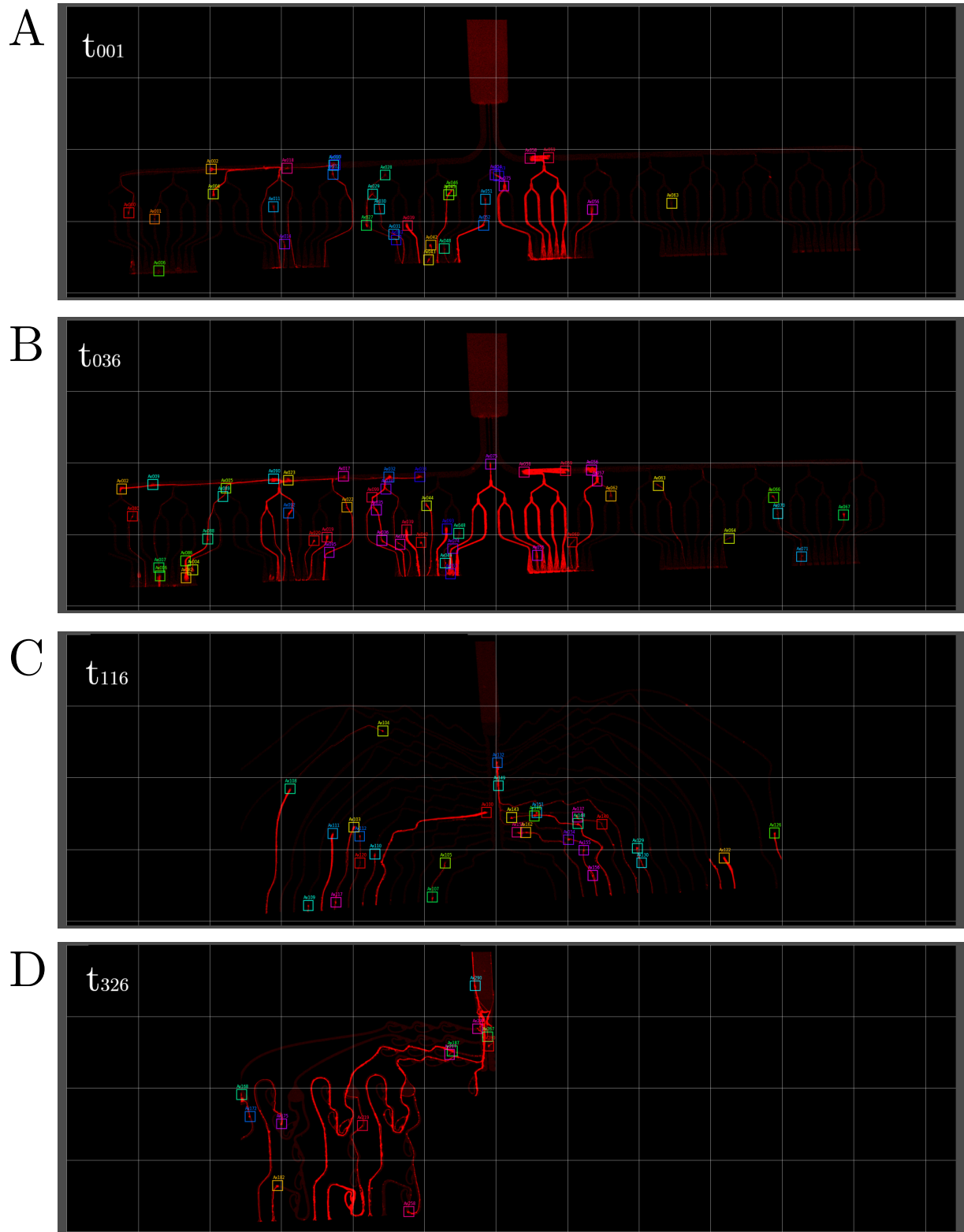


labelled and

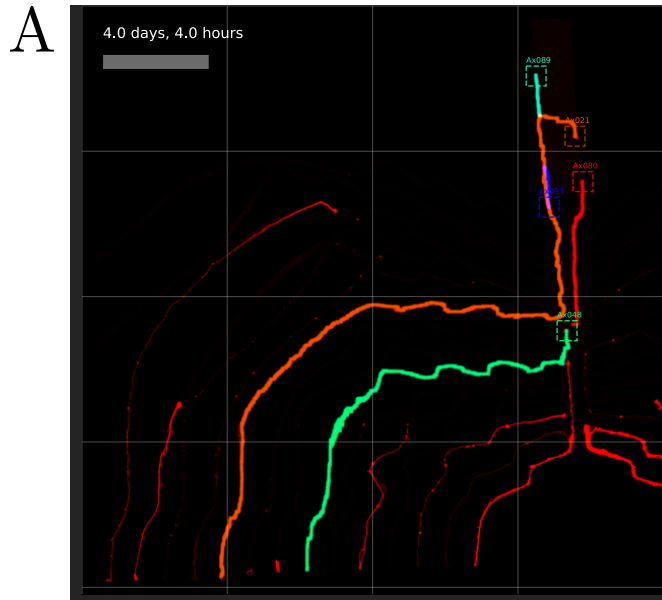
Supplementary Figure 1: Initial timelapse preprocessing steps. **A** A snapshot of the exported video including the relevant metadata of the recording. **B** The napari image viewer interface with the edge segmentation layer in brown. **C** The manually segmented binary mask of the micro channels in non-black, the output channel in green, and the exiting channels in brown. The green dot in the output channel marks the target point of the PDMS design.



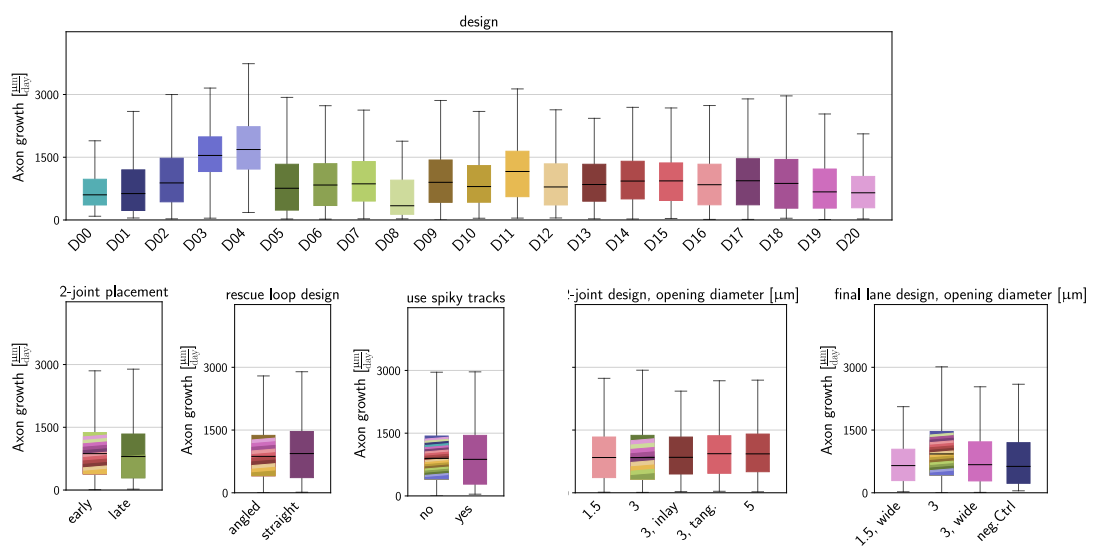
Supplementary Figure 2: Axon growth cone labelling. **A** shows a snapshot of the napari image viewer during labelling. Each circle represents a growth cone label, the color corresponds to the identity. Each axon identity is saved as a napari-Points layer which are listed on the left. **B** illustrates the axon identify lifetime. A green point on this pixel map indicates that a label exists for the matching axon identity and frame. The three clusters originate from the concatenation of three PDMS microstructure timelapse videos.



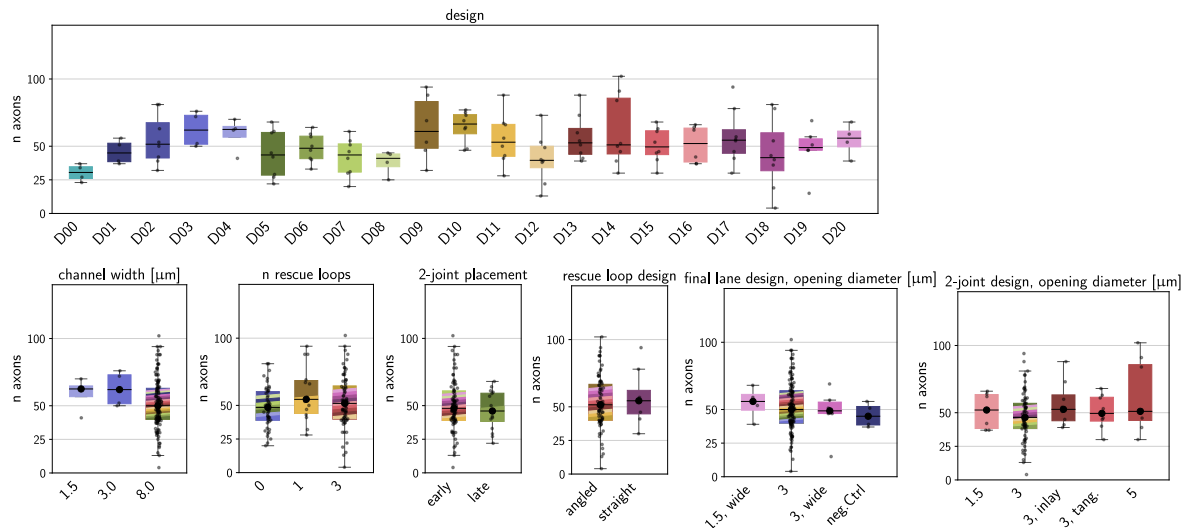
Supplementary Figure 3: Labelled training data examples. **A** shows the first frame of the training data sequence. Each box represents a growth cone, the color indicates the identity over consecutive frames. **B** shows the last frame of Dataset1. **C** shows the last frame of Dataset2, PDMS micro structure 1 (compare Table 2). **D** shows the last frame of Dataset2, PDMS micro structure 2. Gridsize = 317 μm .



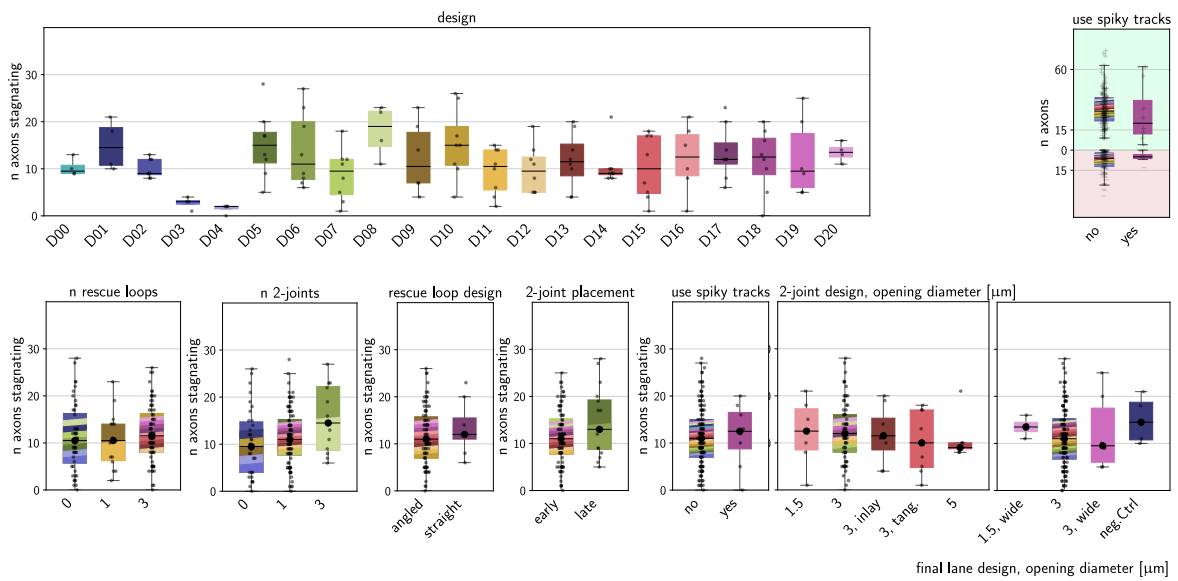
Supplementary Figure 4: Axon reconstruction from growth cone track. **A** For clarity, only a subset of identified axons is drawn.



Supplementary Figure 5: Axonal growth velocity. Significance is not shown.



Supplementary Figure 6: Axon outgrowth frequency. Significance is not shown.



Supplementary Figure 7: Number of axons stagnating. Significance is not shown. Top right plot shows counts of axons growing incorrectly (red), and correctly (green) for a feature that did not show significant effects.

References

- Mead, Carver (1989). *Analog VLSI Implementation of Neural Systems*. Ed. by Carver Mead and Mohammed Ismail. Vol. 80. Springer US. ISBN: 978-1-4612-8905-0. DOI: 10.1007/978-1-4613-1639-8. URL: <http://link.springer.com/10.1007/978-1-4613-1639-8>.
- Durand, Dominique M. (Sept. 2006). "What is Neural Engineering?" In: *Journal of Neural Engineering* 4 (4), E01. ISSN: 1741-2552. DOI: 10.1088/1741-2552/4/4/E01. URL: <https://iopscience.iop.org/article/10.1088/1741-2552/4/4/E01>
<https://iopscience.iop.org/article/10.1088/1741-2552/4/4/E01/meta>.
- Maynard, Edwin M., Craig T. Nordhausen, and Richard A. Normann (1997). "The Utah intracortical Electrode Array: a recording structure for potential brain-computer interfaces". In: *Electroencephalography and clinical neurophysiology* 102 (3), pp. 228–239. ISSN: 0013-4694. DOI: 10.1016/S0013-4694(96)95176-0. URL: <https://pubmed.ncbi.nlm.nih.gov/9129578/>.
- Jun, James J. et al. (Nov. 2017). "Fully integrated silicon probes for high-density recording of neural activity". In: *Nature* 2017 551:7679 551 (7679), pp. 232–236. ISSN: 1476-4687. DOI: 10.1038/nature24636. URL: <https://www.nature.com/articles/nature24636>.
- Stevenson, Ian H. and Konrad P. Kording (Jan. 2011). "How advances in neural recording affect data analysis". In: *Nature Neuroscience* 2011 14:2 14 (2), pp. 139–142. ISSN: 1546-1726. DOI: 10.1038/nn.2731. URL: <https://www.nature.com/articles/nn.2731>.
- Herrington, Todd M., Jennifer J. Cheng, and Emad N. Eskandar (Jan. 2016). "Mechanisms of deep brain stimulation". In: *Journal of Neurophysiology* 115 (1), pp. 19–38. ISSN: 15221598. DOI: 10.1152/JN.00281.2015/ASSET/IMAGES/LARGE/Z9K0011634190006. JPEG. URL: <https://journals.physiology.org/doi/abs/10.1152/jn.00281.2015>.
- Tong, Wei et al. (Mar. 2020). "Stimulation Strategies for Improving the Resolution of Retinal Prostheses". In: *Frontiers in Neuroscience* 14, p. 262. ISSN: 1662453X. DOI: 10.3389/FNINS.2020.00262/BIBTEX.
- Tresco, Patrick A. and Brent D. Winslow (2011). "The Challenge of Integrating Devices into the Central Nervous System". In: *Critical Reviews in Biomedical Engineering* 39 (1), pp. 29–44. ISSN: 0278-940X. DOI: 10.1615/CRITREVBIOMEDENG.V39.I1.30. URL: <https://www.dl.begellhouse.com/journals/4b27cbfc562e21b8,7d5e987c7e576915,1e61f79c5183ad8b.html>.
- Saxena, Tarun et al. (July 2013). "The impact of chronic blood-brain barrier breach on intracortical electrode function". In: *Biomaterials* 34 (20), pp. 4703–4713. ISSN: 01429612. DOI: 10.1016/j.biomaterials.2013.03.007.
- Grill, Warren M., Sharon E. Norman, and Ravi V. Bellamkonda (July 2009). "Implanted Neural Interfaces: Biochallenges and Engineered Solutions". In: <http://dx.doi.org/10.1146/annurev-bioeng-061008-124927> 11, pp. 1–24. ISSN: 15239829. DOI: 10.1146/ANNUREV-BIOENG-061008-124927. URL: <https://www.annualreviews.org/doi/abs/10.1146/annurev-bioeng-061008-124927>.
- Polikov, Vadim S., Patrick A. Tresco, and William M. Reichert (Oct. 2005). "Response of brain tissue to chronically implanted neural electrodes". In: *Journal of Neuroscience Methods* 148 (1), pp. 1–18. ISSN: 0165-0270. DOI: 10.1016/J.JNEUMETH.2005.08.015.

- Zemelman, Boris V. et al. (Jan. 2002). "Selective photostimulation of genetically chARGed neurons". In: *Neuron* 33 (1), pp. 15–22. ISSN: 0896-6273. DOI: 10.1016/S0896-6273(01)00574-8. URL: <https://pubmed.ncbi.nlm.nih.gov/11779476/>.
- Boyden, Edward S. et al. (Aug. 2005). "Millisecond-timescale, genetically targeted optical control of neural activity". In: *Nature Neuroscience* 2005 8:9 8 (9), pp. 1263–1268. ISSN: 1546-1726. DOI: 10.1038/nn1525. URL: <https://www.nature.com/articles/nn1525>.
- Mendoza, Skyler D., Yasmine El-Shamayleh, and Gregory D. Horwitz (May 2017). "AAV-mediated delivery of optogenetic constructs to the macaque brain triggers humoral immune responses". In: *Journal of Neurophysiology* 117 (5), pp. 2004–2013. ISSN: 15221598. DOI: 10.1152/JN.00780.2016/ASSET/IMAGES/LARGE/Z9K0051740960006. JPEG. URL: <https://journals.physiology.org/doi/abs/10.1152/jn.00780.2016>.
- Stieglitz, T. et al. (Aug. 2002). "A biohybrid system to interface peripheral nerves after traumatic lesions: design of a high channel sieve electrode". In: *Biosensors and Bioelectronics* 17 (8), pp. 685–696. ISSN: 0956-5663. DOI: 10.1016/S0956-5663(02)00019-2.
- Rochford, Amy E. et al. (Apr. 2020). "When Bio Meets Technology: Biohybrid Neural Interfaces". In: *Advanced Materials* 32 (15), p. 1903182. ISSN: 1521-4095. DOI: 10.1002/ADMA.201903182. URL: <https://onlinelibrary.wiley.com/doi/full/10.1002/adma.201903182> <https://onlinelibrary.wiley.com/doi/abs/10.1002/adma.201903182>.
- Purcell, E. K. et al. (Mar. 2009). "In vivo evaluation of a neural stem cell-seeded prosthesis". In: *Journal of Neural Engineering* 6 (2), p. 026005. ISSN: 1741-2552. DOI: 10.1088/1741-2560/6/2/026005. URL: <https://iopscience.iop.org/article/10.1088/1741-2560/6/2/026005> <https://iopscience.iop.org/article/10.1088/1741-2560/6/2/026005/meta>.
- Faveri, Sara De et al. (Apr. 2014). "Bio-inspired hybrid microelectrodes: A hybrid solution to improve long-term performance of chronic intracortical implants". In: *Frontiers in Neuroengineering* 7 (APR), p. 7. ISSN: 16626443. DOI: 10.3389/FNENG.2014.00007/BIBTEX.
- Tang-Schomer, Min D. et al. (Apr. 2014). "Film-Based Implants for Supporting Neuron-Electrode Integrated Interfaces for The Brain". In: *Advanced Functional Materials* 24 (13), pp. 1938–1948. ISSN: 1616-3028. DOI: 10.1002/ADFM.201303196. URL: <https://onlinelibrary.wiley.com/doi/full/10.1002/adfm.201303196> <https://onlinelibrary.wiley.com/doi/abs/10.1002/adfm.201303196> <https://onlinelibrary.wiley.com/doi/10.1002/adfm.201303196>.
- Adewole, Dayo O. et al. (Jan. 2021). "Development of optically controlled "living electrodes" with long-projecting axon tracts for a synaptic brain-machine interface". In: *Science Advances* 7 (4). ISSN: 23752548. DOI: 10.1126/SCIADV.AAY5347/SUPPLFILE/AAY5347_SM.PDF. URL: <https://www.science.org/doi/abs/10.1126/sciadv.aay5347>.
- Bourne, Rupert R.A. et al. (Feb. 2021). "Trends in prevalence of blindness and distance and near vision impairment over 30 years: an analysis for the Global Burden of Disease Study". In: *The Lancet. Global health* 9 (2), e130–e143. ISSN: 2214-109X. DOI: 10.1016/S2214-109X(20)30425-3. URL: <https://pubmed.ncbi.nlm.nih.gov/33275950/>.
- Tybrandt, Klas et al. (Apr. 2018). "High-Density Stretchable Electrode Grids for Chronic Neural Recording". In: *Advanced Materials* 30 (15), p. 1706520. ISSN: 1521-4095. DOI:

- 10.1002/ADMA.201706520. URL: <https://onlinelibrary.wiley.com/doi/full/10.1002/adma.201706520>
- Douglas, R. J. and K. A. Martin (Aug. 1991). "A functional microcircuit for cat visual cortex". In: *The Journal of physiology* 440 (1), pp. 735–769. ISSN: 0022-3751. DOI: 10.1113/JPHYSIOL.1991.SP018733. URL: <https://pubmed.ncbi.nlm.nih.gov/1666655/>.
- Markram, Henry et al. (Jan. 1997). "Regulation of synaptic efficacy by coincidence of postsynaptic APs and EPSPs". In: *Science* 275 (5297), pp. 213–215. ISSN: 00368075. DOI: 10.1126/SCIENCE.275.5297.213
- Yamamoto, H. et al. (July 2016). "Unidirectional signal propagation in primary neurons micropatterned at a single-cell resolution". In: *Applied Physics Letters* 109 (4). ISSN: 00036951. DOI: 10.1063/1.4959836.
- Forró, Csaba et al. (Dec. 2018). "Modular microstructure design to build neuronal networks of defined functional connectivity". In: *Biosensors and Bioelectronics* 122, pp. 75–87. ISSN: 0956-5663. DOI: 10.1016/J.BIOS.2018.08.075.
- Millet, Larry J. and Martha U. Gillette (Dec. 2012). "New perspectives on neuronal development via microfluidic environments". In: *Trends in neurosciences* 35 (12), pp. 752–761. ISSN: 1878-108X. DOI: 10.1016/J.TINS.2012.09.001. URL: <https://pubmed.ncbi.nlm.nih.gov/23031246/>.
- Neto, Estrela et al. (Nov. 2016). "Compartmentalized Microfluidic Platforms: The Unrivaled Breakthrough of In Vitro Tools for Neurobiological Research". In: *The Journal of neuroscience : the official journal of the Society for Neuroscience* 36 (46), pp. 11573–11584. ISSN: 1529-2401. DOI: 10.1523/JNEUROSCI.1748-16.2016. URL: <https://pubmed.ncbi.nlm.nih.gov/27852766/>.
- Millet, Larry J. et al. (2007). "Microfluidic devices for culturing primary mammalian neurons at low densities". In: *Lab on a chip* 7 (8), pp. 987–994. ISSN: 1473-0197. DOI: 10.1039/B705266A. URL: <https://pubmed.ncbi.nlm.nih.gov/17653340/>.
- Francisco, Herbert et al. (Aug. 2007). "Regulation of Axon Guidance and Extension by 3-Dimensional Constraints". In: *Biomaterials* 28 (23), p. 3398. ISSN: 01429612. DOI: 10.1016/J.BIOMATERIALS.2007.04.015. URL: /pmc/articles/PMC1952179//pmc/articles/PMC1952179/?report=abstract
- Feber, Joost Le et al. (2015). "Barbed channels enhance unidirectional connectivity between neuronal networks cultured on multi electrode arrays". In: *Frontiers in Neuroscience* 9 (NOV), p. 412. ISSN: 1662453X. DOI: 10.3389/FNINS.2015.00412/BIBTEX.
- Peyrin, Jean Michel et al. (Oct. 2011). "Axon diodes for the reconstruction of oriented neuronal networks in microfluidic chambers". In: *Lab on a Chip* 11 (21), pp. 3663–3673. ISSN: 14730189. DOI: 10.1039/C1LC20014C. URL: <https://pubs.rsc.org/en/>

- content/articlehtml/2011/1c/c11c20014chhttps://pubs.rsc.org/en/content/articlelanding/2011/1c/c11c20014c.
- Pirlo, R. K. et al. (Mar. 2011). “Biochip/laser cell deposition system to assess polarized axonal growth from single neurons and neuron/glia pairs in microchannels with novel asymmetrical geometries”. In: *Biomicrofluidics* 5 (1), p. 013408. ISSN: 19321058. DOI: 10.1063/1.3552998. URL: <https://aip.scitation.org/doi/abs/10.1063/1.3552998>.
- Na, Sangcheol et al. (Mar. 2017). “Microfluidic neural axon diode”. In: *Technology* 04 (04), pp. 240–248. ISSN: 2339-5478. DOI: 10.1142/S2339547816500102.
- Renault, Renaud et al. (June 2016). “Asymmetric axonal edge guidance: a new paradigm for building oriented neuronal networks”. In: *Lab on a Chip* 16 (12), pp. 2188–2191. ISSN: 14730189. DOI: 10.1039/C6LC00479B. URL: <https://pubs.rsc.org/en/content/articlehtml/2016/1c/c6lc00479bhttps://pubs.rsc.org/en/content/articlelanding/2016/1c/c6lc00479b>.
- Holloway, Paul M. et al. (Apr. 2019). “Asymmetric confinement for defining outgrowth directionality”. In: *Lab on a Chip* 19 (8), pp. 1484–1489. ISSN: 1473-0189. DOI: 10.1039/C9LC00078J. URL: <https://pubs.rsc.org/en/content/articlehtml/2019/1c/c9lc00078jhttps://pubs.rsc.org/en/content/articlelanding/2019/1c/c9lc00078j>.
- Gladkov, Arseniy et al. (Nov. 2017). “Design of Cultured Neuron Networks in vitro with Predefined Connectivity Using Asymmetric Microfluidic Channels”. In: *Scientific Reports* 2017 7:1 7 (1), pp. 1–14. ISSN: 2045-2322. DOI: 10.1038/s41598-017-15506-2. URL: <https://www.nature.com/articles/s41598-017-15506-2>.
- Isomura, Takuya et al. (Nov. 2015). “Signal transfer within a cultured asymmetric cortical neuron circuit”. In: *Journal of Neural Engineering* 12 (6), p. 066023. ISSN: 1741-2552. DOI: 10.1088/1741-2560/12/6/066023. URL: <https://iopscience.iop.org/article/10.1088/1741-2560/12/6/066023https://iopscience.iop.org/article/10.1088/1741-2560/12/6/066023/meta>.
- Braso, Guillem and Laura Leal-Taixe (Dec. 2019). “Learning a Neural Solver for Multiple Object Tracking”. In: *Proceedings of the IEEE Computer Society Conference on Computer Vision and Pattern Recognition*, pp. 6246–6256. ISSN: 10636919. DOI: 10.1109/CVPR42600.2020.00628. URL: <https://arxiv.org/abs/1912.07515v2>.
- Krizhevsky, Alex, Ilya Sutskever, and Geoffrey E. Hinton (May 2017). “ImageNet classification with deep convolutional neural networks”. In: *Communications of the ACM* 60 (6), pp. 84–90. ISSN: 15577317. DOI: 10.1145/3065386. URL: <https://dl.acm.org/doi/abs/10.1145/3065386>.
- Girshick, Ross (Apr. 2015). “Fast R-CNN”. In: *arXiv*. URL: <https://arxiv.org/abs/1504.08083>.
- Ren, Shaoqing et al. (June 2015). “Faster R-CNN: Towards Real-Time Object Detection with Region Proposal Networks”. In: *arXiv*. URL: <https://arxiv.org/abs/1506.01497>.
- Redmon, Joseph et al. (June 2015). “You Only Look Once: Unified, Real-Time Object Detection”. In: *Proceedings of the IEEE Computer Society Conference on Computer Vision and Pattern Recognition* 2016-December, pp. 779–788. ISSN: 10636919. DOI: 10.1109/CVPR.2016.91. URL: <https://arxiv.org/abs/1506.02640v5>.
- Redmon, Joseph and Ali Farhadi (Apr. 2018). “YOLOv3: An Incremental Improvement”. In: *arXiv*. URL: <https://arxiv.org/abs/1804.02767>.

- Long, Xiang et al. (July 2020). "PP-YOLO: An Effective and Efficient Implementation of Object Detector". In: *arXiv*. URL: <http://arxiv.org/abs/2007.12099>.
- Bewley, Alex et al. (Aug. 2016). "Simple online and realtime tracking". In: *Proceedings - International Conference on Image Processing, ICIP* 2016-August, pp. 3464–3468. ISSN: 15224880. DOI: [10.1109/ICIP.2016.7533003](https://doi.org/10.1109/ICIP.2016.7533003).
- Kuhn, Harold W (Mar. 1955). "The Hungarian Method for the Assignment Problem". In: *Naval Research Logistics Quarterly* 2 (1–2), pp. 83–97. DOI: [10.1002/nav.3800020109](https://doi.org/10.1002/nav.3800020109).
- Wang, Congchao, Yizhi Wang, and Guoqiang Yu (Nov. 2019). "Efficient Global Multi-object Tracking Under Minimum-cost Circulation Framework". In: *IEEE Transactions on Pattern Analysis and Machine Intelligence*, pp. 1–1. ISSN: 0162-8828. DOI: [10.1109/tpami.2020.3026257](https://doi.org/10.1109/tpami.2020.3026257). URL: <https://arxiv.org/abs/1911.00796v2>.
- Wojke, Nicolai, Alex Bewley, and Dietrich Paulus (Mar. 2017). "Simple Online and Real-time Tracking with a Deep Association Metric". In: *Proceedings - International Conference on Image Processing, ICIP* 2017-September, pp. 3645–3649. ISSN: 15224880. DOI: [10.1109/ICIP.2017.8296962](https://doi.org/10.1109/ICIP.2017.8296962). URL: <https://arxiv.org/abs/1703.07402v1>.
- Yoon, Kwangjin et al. (Jan. 2019). "Data Association for Multi-Object Tracking via Deep Neural Networks". In: *Sensors 2019, Vol. 19, Page 559* 19 (3), p. 559. ISSN: 14248220. DOI: [10.3390/S19030559](https://doi.org/10.3390/S19030559). URL: <https://www.mdpi.com/1424-8220/19/3/559>.
- Tsai, Hsieh Fu et al. (Jan. 2019). "Usiigaci: Instance-aware cell tracking in stain-free phase contrast microscopy enabled by machine learning". In: *SoftwareX* 9, pp. 230–237. ISSN: 2352-7110. DOI: [10.1016/J.SOFTX.2019.02.007](https://doi.org/10.1016/J.SOFTX.2019.02.007).
- Anjum, Samreen and Danna Gurari (June 2020). "CTMC: Cell tracking with mitosis detection dataset challenge". In: *IEEE Computer Society Conference on Computer Vision and Pattern Recognition Workshops* 2020-June, pp. 4228–4237. ISSN: 21607516. DOI: [10.1109/CVPRW50498.2020.00499](https://doi.org/10.1109/CVPRW50498.2020.00499).
- Welshhans, Kristy and Gary J. Bassell (July 2011). "Netrin-1-Induced Local β -Actin Synthesis and Growth Cone Guidance Requires Zipcode Binding Protein 1". In: *Journal of Neuroscience* 31 (27), pp. 9800–9813. ISSN: 0270-6474. DOI: [10.1523/JNEUROSCI.0166-11.2011](https://doi.org/10.1523/JNEUROSCI.0166-11.2011). URL: <https://www.jneurosci.org/content/31/27/9800>.
- Sofroniew, Nicholas et al. (Oct. 2021). "napari/napari: 0.4.12rc2". In: DOI: [10.5281/ZENODO.5587893](https://doi.org/10.5281/ZENODO.5587893). URL: <https://zenodo.org/record/5587893>.
- Ioffe, Sergey and Christian Szegedy (Feb. 2015). "Batch Normalization: Accelerating Deep Network Training by Reducing Internal Covariate Shift". In: *32nd International Conference on Machine Learning, ICML* 2015 1, pp. 448–456. URL: <https://arxiv.org/abs/1502.03167v3>.
- Maas, Andrew L, Awni Y Hannun, and Andrew Y Ng (2013). "Rectifier nonlinearities improve neural network acoustic models". In:
- Bodla, Navaneeth et al. (Apr. 2017). "Soft-NMS – Improving Object Detection With One Line of Code". In: *Proceedings of the IEEE International Conference on Computer Vision* 2017-October, pp. 5562–5570. ISSN: 15505499. DOI: [10.1109/ICCV.2017.593](https://doi.org/10.1109/ICCV.2017.593). URL: <https://arxiv.org/abs/1704.04503v2>.
- Kingma, Diederik P. and Jimmy Lei Ba (Dec. 2014). "Adam: A Method for Stochastic Optimization". In: *3rd International Conference on Learning Representations, ICLR* 2015 - Conference Track Proceedings. URL: <https://arxiv.org/abs/1412.6980v9>.

Hart, Peter E., Nils J. Nilsson, and Bertram Raphael (1968). “A Formal Basis for the Heuristic Determination of Minimum Cost Paths”. In: *IEEE Transactions on Systems Science and Cybernetics* 4 (2), pp. 100–107. ISSN: 21682887. DOI: 10.1109/TSSC.1968.300136.